Received Date: 02-Oct-2016

Revised Date: 12-Dec-2016

Accepted Date: 27-Dec-2016

Article Type: Research Article

Statistical image-domain multi-material decomposition for dual-energy CT

Yi Xue[1,2], Ruoshui Ruan[3], Xiuhua Hu[1], Yu Kuang[4], Jing Wang[1], Yong Long[3, a)] and Tianye Niu[1,2, a)]

[1]*Sir Run Run Shaw Hospital, Zhejiang University School of Medicine; Institute of Translational Medicine, Zhejiang University, Hangzhou, Zhejiang, 310009, China*

[2]*Key Laboratory of Biomedical Engineering of Ministry of Education, Zhejiang University, Hangzhou, Zhejiang, 310009, China*

[3]*University of Michigan–Shanghai Jiao Tong University Joint Institute, Shanghai Jiao Tong University, Shanghai, 200240, China*

[4]*Department of Medical Physics, University of Nevada, Las Vegas, 4505 S Maryland Pkwy, Box 453037, Las Vegas, NV 89154-3037, USA*

a） Author to whom correspondence should be addressed. Electronic mails: tyniu@zju.edu.cn (Tianye Niu), and yong.long@sjtu.edu.cn (Yong Long).

The authors declare that they do not have any conflict of interest.

This is the author manuscript accepted for publication and has undergone full peer review but has not been through the copyediting, typesetting, pagination and proofreading process, which may lead to differences between this version and the Version of Record. Please cite this article as doi: 10.1002/mp.12096

This article is protected by copyright. All rights reserved

Author Manuscript

Purpose: Dual-energy CT (DECT) enhances tissue characterization because of its basis material decomposition capability. In addition to conventional two-material decomposition from DECT measurements, multi-material decomposition (MMD) is required in many clinical applications. To solve the ill-posed problem of reconstructing multiple-material images from dual-energy measurements, additional constraints are incorporated into the formulation, including volume and mass conservation and the assumptions that at most three materials in each pixel and various material types among pixels. The recently proposed flexible image-domain MMD method decomposes pixels sequentially into multiple basis materials using direct inversion scheme and leads to magnified noise in the material images. In this paper, we propose a statistical image-domain MMD method for DECT to suppress the noise.

Methods: The proposed method applies penalized weighted least-square (PWLS) reconstruction with a negative log-likelihood term and edge-preserving regularization for each material. The statistical weight is determined by a data-based method accounting for the noise variance of high- and low-energy CT images. We apply the optimization transfer principles to design a serial of pixel-wise separable quadratic surrogates (PWSQS) functions which monotonically decrease the cost function. The separability in each pixel enables simultaneous update of all pixels.

Results: The proposed method is evaluated on a digital phantom, Catphan©600 phantom and three patients (pelvis, head and thigh). We also implement the direct inversion and low-pass filtration methods for comparison purpose. Compared with the direct inversion method, the proposed method reduces noise standard deviation (STD) in soft-tissue by 95.35% in the digital phantom study, by 88.01% in the Catphan©600 phantom study, by 92.45% in the pelvis patient study, by 60.21% in the head patient study, and by 81.22% in the thigh patient study, respectively. The overall volume fraction accuracy is improved by around 6.85%. Compared with the low-pass filtration method, the root-mean-square percentage error (RMSE(%)) of electron densities in the Catphan©600 phantom is decreased by 20.89%. At modulation transfer function (MTF) magnitude decreased to 50%, the proposed method increases the spatial resolution by an overall factor of 1.64 on the digital phantom, and 2.16 on the Catphan©600 phantom. The overall volume fraction accuracy is increased by 6.15%.

Conclusions: We proposed a statistical image-domain MMD method using DECT measurements.

This article is protected by copyright. All rights reserved

Author Manuscript

The method successfully suppresses the magnified noise while faithfully retaining the quantification accuracy and anatomical structure in the decomposed material images. The proposed method is practical and promising for advanced clinical applications using DECT imaging.

Key words: Dual-energy CT (DECT), Image-domain, Multi-material decomposition (MMD), Noise suppression, Optimization transfer, Penalized weighted least-square (PWLS).

1. Introduction

Spectral CT enhances tissue characterization because of its basis materials decomposition capability.[1-9] In essence, two basis materials with various linear attenuation coefficients (e.g. bone and soft-tissue) can be reconstructed using dual-energy CT (DECT) technique accurately[4-9]. In clinical applications, three or more component images are usually required[1-3, 10, 11]. For example, liver-fat quantification requires four-material composition: liver tissue, blood, fat and contrast agent[1-3]. One method to achieve this is using expensive hardware, e.g., energy-sensitive photon-counting detectors, to acquire multi-energy projection data. This paper proposes a multi-material decomposition (MMD) method using conventional dual-energy measurements which are available from clinical DECT scanners. For example, dual-energy measurements can be acquired from fast kVp-switching[12, 13], dual-source[13-15] or dual-layer detectors[13, 16] DECT scanners.

DECT methods can be classified into three categories: projection-domain, image-domain and direct reconstruction methods[17]. Projection-domain methods decompose DECT measurements into sinograms of basis materials and generate material images using conventional reconstruction algorithms. These methods avoid beam-hardening artifacts because the material specific projections are estimated prior to image reconstruction[5, 18]. One major challenge for this type of methods is the calibration of spectral transmission model which is nonlinear and computationally expensive. Image-domain methods apply standard reconstruction techniques to obtain low- and high-energy CT images, and decompose them into basis material images using linear approximation of decomposition process[1-4, 19, 20]. Mendonça *et al.* proposed an image-domain pixel-wise MMD method for DECT[1, 2]. This method assumes three basis materials at the most

This article is protected by copyright. All rights reserved

Author Manuscript

within each pixel and the material types alter among the pixels. The mass and volume conservation are also included as the constraints. It suffers from magnified noise in the decomposed basis images since direct inversion at each pixel is used to estimate volume fractions of basis materials. Long and Fessler proposed a direct MMD method for DECT using penalized-likelihood (PL) reconstruction with edge-preserving regularization for each material[3]. This method has advantages of modeling the physics of spectral transmission exactly, incorporating similar constrains as the method proposed by Mendonça *et al.* [1, 2] to its CT object model, and significantly decreasing noise and cross-artifacts in the decomposed material images. Nevertheless, it is computationally expensive due to the repeated forward projection of material images and backward projection of the measurements at low and high energies and the modeling of poly-energetic spectra. We also proposed an image-domain method[4], which is an iterative dual-material decomposition with noise suppression using least-square estimation and edge-preserving regularization. In clinical applications, the detected objects have more compositions and the two-material decomposition sometimes is inadequate to fully meet the clinical needs.

The decomposition procedure of DECT measurements is highly sensitive to noise fluctuation due to the overlap of x-ray spectra at low and high energies. To tackle the obstacle, we propose an improved decomposition method to achieve the multi-material decomposition (MMD) in this paper. Assuming similar constraints applied in pervious MMD methods for DECT,[1-3] we investigate noise suppression in image-domain MMD method. The cost function of the proposed method is in the form of penalized weighted least-square (PWLS) estimation with edge-preserving regularization. The statistical weight is determined by a data-based method accounting for the noise variance of high- and low-energy CT images. The optimization transfer principle is applied to design a pixel-wise separable quadratic surrogate (PWSQS) function in each iteration to reduce the cost function monotonically.[3] The separability in each pixel enables simultaneous update of all pixels. The proposed method is evaluated on one digital phantom, one physical phantom (i.e., Catphan©600 evaluation phantom) and three sets of patient data. Compared with the image-domain direct inversion method, the proposed method can significantly suppress noise while faithfully retaining the anatomical structure and decomposition accuracy.

2. Methods

This article is protected by copyright. All rights reserved

Author Manuscript

2.1. Object model for multi-material decomposition (MMD)

Multi-material decomposition (MMD) from DECT measurements is an ill-posed problem since multiple sets of images are estimated from two sets of measurements associated with low and high energies. To solve this ill-posed problem, we apply constraints of volume and mass conservation[1-3, 11], and assume that each pixel contains at most three materials and the material composition, i.e., material-triplet, varies among pixels[1-3].

With mass and volume conservation, the spatially- and energy-dependent attenuation distribution $\vec{\mu}_E$ is

$$\vec{\mu}_E = \sum_{l=1}^{L_0} \mu_{lE}\, \vec{x}_l, \tag{1}$$

where $\vec{x}_l$ denotes the volume fraction image of the *l*-th material and is unitless. L_0 is the total number of basis material types, and μ_{lE} is the linear attenuation coefficient (LAC) of the *l*-th material at energy level *E*. According to the constraints of volume conservation, volume fraction $\vec{x}_l$ satisfies the sum-to-one and box constraints, i.e.,

$$\sum_{l=1}^{L_0} x_{lp} = 1, \forall p, \tag{2}$$

$$a_l \le x_{lp} \le b_l, \forall l, p, \tag{3}$$

where *p* indicates the *p*-th pixel. We relax the lower bound a_l of the box constraint to be slightly smaller than 0, and the upper bound b_l to be slightly greater than 1[3, 21]. Under the assumptions that each pixel contains at most three basis materials and triplet-material composition change among pixels[3] volume fraction $\vec{x}_l$ also satisfies the following constraint,

$$\sum_{l=1}^{L_0} I_{\{x_{lp} \ne 0\}} \le 3, \forall p, \tag{4}$$

where $I_{\{\cdot\}}$ denotes the indicator function, which is 1 if the condition is satisfied and 0 otherwise.

We define Ω as a material triplet library containing all the possible triplets from pre-selected materials of interest[1-3]. The image-domain direct inversion method proposed by Mendonça *et al.* [1, 2] solves the linear system in Eqs. (1) and (2) for a given pixel in the triplet library Ω. If only one solution satisfies the box constraint $0 \le x_l \le 1, \forall l$, the optimal solution is found. If more than one feasible solution exists, the solution with the minimal the Euclidean distance to the LAC pair is selected as the optimal solution from all the triplets in the feasible solution pool. If no feasible solution is found, the box constraint is relaxed to find the possible triplets, and the triplet with minimal Hausdorff distance to the LAC pair is selected as the optimal solution[1]. This method

This article is protected by copyright. All rights reserved

Author Manuscript

yields noisy material images due to the unregularized inversion[3].

2.2. Statistical image-domain multi-material decomposition

To suppress noise in the decomposed material images, we employ a penalized weighted least-square (PWLS) method to estimate multiple material images from high- and low-energy CT images. We model the high- and low-energy CT images as independent Gaussian random variables, i.e.,

$$\mu_{Ep} \sim N\left((\vec{a}_E)^T \vec{x}_p, var(\mu_{Ep})\right). \tag{5}$$

where the measurement μ_{Ep} corresponding to the *p*-th pixel value at energy level *E*, *T* denotes the transpose operator, $\vec{a}_E = [\mu_{1E}, \dots, \mu_{L_0E}]^T$, $\vec{x}_p = [x_{1p}, \dots, x_{L_0p}]^T$ is a vector of L_0 elements at the *p*-th pixel, and $var(\mu_{Ep})$ is the variance. The probability density function (pdf) is

$$p(\mu_{Ep}; \vec{x}_p) = \frac{1}{\sqrt{2\pi var(\mu_{Ep})}} \exp\left(-\frac{(\mu_{Ep} - (\vec{a}_E)^T \vec{x}_p)^2}{2var(\mu_{Ep})}\right). \tag{6}$$

The corresponding negative log-likelihood for independent measurements μ_{Ep} has the form,

$$\begin{aligned} L(\vec{x}) &= -\sum_{E=1}^{2} \sum_{p=1}^{Np} \log\left(p(\mu_{Ep}; \vec{x}_p)\right) \\ &\equiv (A\vec{x} - \vec{\mu})^T V^{-1} (A\vec{x} - \vec{\mu}). \end{aligned} \tag{7}$$

where the symbol $\equiv$ indicates "equal to within irrelevant constants independent of $\vec{x}$". N_p is the total number of pixels in one CT image. The $2N_p \times L_0N_p$ system matrix A is defined as

$$A = A_0 \otimes I_{N_P}, \tag{8}$$

where "$\otimes$" denotes the Kronecker product, the $2 \times L_0$ material decomposition matrix A_0 is

$$A_0 = \begin{pmatrix} \mu_{1H} \dots \mu_{L_0H} \\ \mu_{1L} \dots \mu_{L_0L} \end{pmatrix}. \tag{9}$$

Here I_{N_P} denotes the $N_p \times N_p$ identity matrix. $\vec{\mu} = [\vec{\mu}_H^T \ \vec{\mu}_L^T]^T$ is a $2N_p$ vector where $\vec{\mu}_H$ and $\vec{\mu}_L$ are the high- and low-energy CT images, respectively. $\vec{x} = [\vec{x}_1^T, \dots, \vec{x}_{L_0}^T]^T$ is a L_0N_p vector composed of $\vec{x}_1$,…, $\vec{x}_{L_0}$ basis material images. The statistical weight *V* is a $2N_p \times 2N_p$ diagonal matrix whose diagonal elements are the noise variance of pixels in the high- and low-energy CT images, i.e.,

$$V = diag\left(var(\mu_{H1}), \dots, var(\mu_{HNp}), var(\mu_{L1}), \dots, var(\mu_{LNp})\right). \tag{10}$$

where $var(\mu_{Hp})$ and $var(\mu_{Lp})$ are the statistical noise variance of the *p*-th pixel in the high-

This article is protected by copyright. All rights reserved

Author Manuscript

and low-energy CT images, respectively. The pixel-wise noise variance can be estimated on a serial of CT images acquired from repeated scans on the same object. This method is not practical to implement on clinical patients due to accumulated high radiation dose. In this work, we approximate the noise variance of each pixel in a region composed of homogeneous material of the high/low CT image and calculate the numerical variance as in our previous work[4].

We estimate volume fraction images $\vec{x}$ of basis materials from noisy high- and low-energy CT images by minimizing the PWLS cost function subject to pixel-wise constraints given in Eqs. (2), (3) and (4) as following,

$$\hat{\vec{x}} = \underset{\vec{x}\ subject\ to (2),(3)\&(4)}{argmin} \Psi(\vec{x}). \tag{11}$$

$$\Psi(\vec{x}) \triangleq L(\vec{x}) + R(\vec{x}). \tag{12}$$

The material-wise edge-preserving regularization $R(\vec{x})$ is as following[3, 22],

$$R(\vec{x}) = \sum_{l=1}^{L_0} \beta_l R_l(\vec{x}_l). \tag{13}$$

where the regularizer for the *l*-th material is[3]

$$R_l(\vec{x}_l) = \sum_{p=1}^{N_P} \sum_{k \in N_{lp}} \psi_l(x_{lp} - x_{lk}). \tag{14}$$

Here the potential function ψ_l is a hyperbola[3]

$$\psi_l(t) = \frac{\delta_l^2}{3}\left(\sqrt{1 + 3\left(\frac{t}{\delta_l}\right)^2} - 1\right). \tag{15}$$

and N_{lp} is a neighborhood of pixel x_{lp}. The regularization parameters β_l and δ_l are chosen for different materials separately to achieve desired edge preservation and noise-resolution tradeoff for each material image.

2.3. Optimization Algorithm

Minimizing the cost function $\Psi(\vec{x})$ in Eq. (12) directly is difficult because of the non-convex constraints on each pixel. We thus apply the optimization transfer principles[23-26] to find a serial of pixel-wise separable quadratic surrogate (PWSQS) functions $\phi^{(n)}(\vec{x})$ at each iteration to decrease the cost function monotonically[3]. The separability in pixels enables parallelization of the PWSQS algorithm. The PWSQS function $\phi^{(n)}(\vec{x})$ at the n-th iteration is:

$$\phi^{(n)}(\vec{x}) \equiv \sum_{p=1}^{N_p} \phi_p^{(n)}(\vec{x}_p), \tag{16}$$

where $\phi_p^{(n)}(\vec{x}_p)$ denotes the PWSQS function of the *p*-th pixel. We rewrite the data fidelity term $L(\vec{x})$ in Eq. (7) to show that it is a pixel-wise separable quadratic function as follows,

This article is protected by copyright. All rights reserved

Author Manuscript

$$L(\vec{x}) = \sum_{p=1}^{N_p} L_p(\vec{x}_p). \tag{17}$$

where

$$L_p(\vec{x}_p) = (A_0\vec{x}_p - \vec{\mu}_p)^T V_p^{-1}(A_0\vec{x}_p - \vec{\mu}_p) \ . \tag{18}$$

Here $V_p = diag\left(var(\mu_{Hp}),\ var(\mu_{Lp})\right)$ and $\vec{\mu}_p = [\mu_{Hp}\ \mu_{Lp}]^T$.

Similar to our previous work,[3] we derive a PWSQS function for the penalty term by applying De Pierro's additive convexity trick[23, 27, 28] and use Huber's optimal curvature[29] for the potential function $\psi_l(t)$. The PWSQS function for the penalty term in Eq. (13) is:

$$R^{(n)}(\vec{x}) = \sum_{p=1}^{N_p} R_p^{(n)}(\vec{x}_p). \tag{19}$$

where

$$R_p^{(n)}(\vec{x}_p) = R\left(\vec{x}_p^{(n)}\right) + (\dot{R}_p^{(n)})^T\left(\vec{x}_p - \vec{x}_p^{(n)}\right) + \frac{1}{2}\left(\vec{x}_p - \vec{x}_p^{(n)}\right)^T H_{Rp}^{(n)}\left(\vec{x}_p - \vec{x}_p^{(n)}\right). \tag{20}$$

Here $\dot{R}_p^{(n)}$ and $H_{Rp}^{(n)}$ are the gradient and Hessian of the penalty term about $\vec{x}_p$, respectively, and

$$\dot{R}_p^{(n)} = \left[\beta_1 \frac{\partial}{\partial x_{1p}} R_1\left(\vec{x}_1^{(n)}\right), \dots, \beta_{L_0} \frac{\partial}{\partial x_{L_0 p}} R_{L_0}\left(\vec{x}_{L_0}^{(n)}\right)\right]^T, \tag{21}$$

where

$$\frac{\partial}{\partial x_{lp}} R_l\left(\vec{x}_l^{(n)}\right) = \sum_{k\in N_{lp}} \dot{\psi}_l\left(x_{lp}^{(n)} - x_{lk}^{(n)}\right), l = 1, \dots, L_0. \tag{22}$$

$$H_{Rp}^{(n)} \triangleq diag\left\{4\beta_l \sum_{k\in N_{lp}} \omega_{\psi_l}\left(x_{lp}^{(n)} - x_{lk}^{(n)}\right)\right\},\ where\ \omega_{\psi_l}(t) \triangleq \dot{\psi}_l(t)/t. \tag{23}$$

Combining the PWSQS functions for the data fidelity term and regularization term, we have the PWSQS function for the cost function at the n-th iteration as follows:

$$\begin{aligned}\phi_p^{(n)}(\vec{x}_p) &= L_p(\vec{x}_p) + R_p^{(n)}(\vec{x}_p) \\ &\equiv \frac{1}{2}\vec{x}_p^T H \vec{x}_p + \vec{q}^T \vec{x}_p,\end{aligned} \tag{24}$$

where the Hessian and gradient are

$$H = 2A_0^T V_P^{-1} A_0 + H_{Rp}^{(n)}, \tag{25}$$

$$\vec{q} = 2A_0^T V_P^{-1} A_0 \vec{x}_p^{(n)} - 2A_0^T V_P^{-1}\vec{\mu}_p + \dot{R}_p^{(n)} - H^T \vec{x}_p^{(n)}. \tag{26}$$

To enforce the constraint in Eq. (4), we loop over all the possible triplets in the triplet library Ω and determine the optimal one for each pixel as the triplet minimizing the surrogate of that pixel[3]. For each triplet $\tau = (i, j, k) \in \Omega$, the surrogate degenerates to a quadratic function of a

This article is protected by copyright. All rights reserved

Author Manuscript

vector with three unknowns, $\vec{x}_p(\tau) \triangleq [x_{ip},\ x_{jp},\ x_{kp}]^T$. Optimizing the degenerated quadratic surrogate under constraints in Eqs. (2) and (3) is a classical convex quadratic programming problem[3], i.e.,

$$\begin{aligned} \hat{\vec{x}}_p(\tau) &= \underset{\vec{x}_p(\tau)\ subject\ to\ (2)\ \&\ (3)}{argmin} \phi_p^{(n)}\left(\vec{x}_p(\tau)\right) \\ \phi_p^{(n)}\left(\vec{x}_p(\tau)\right) &\equiv \frac{1}{2}\vec{x}_p^T(\tau)H(\tau)\vec{x}_p(\tau) + \vec{q}^T(\tau)\vec{x}_p(\tau) \\ s.t. &\begin{cases} \sum_{l=1}^{L_0} x_{lp} = 1, \\ a_l \le x_{lp} \le b_l. \end{cases} \end{aligned} \tag{27}$$

where $H(\tau)$ and $\vec{q}(\tau)$ are formed from elements in H and $\vec{q}$ with indexes corresponding to $\tau = (i, j, k)$, respectively. We solve the convex quadratic programming problem in Eq. (27) using Generalized Sequential Minimization Algorithm (GSMO)[30]. Table 1 summarizes the pseudocode of the overall PWSQS algorithm.

Table 1. Pseudocode of the pixel-wise separable quadratic surrogate (PWSQS) algorithm

I) Initialize $\vec{x}^{(0)}$ using the results of the direct inversion method.[1, 2]

II) **For each iteration** n = 1,…, Niter

i) Compute Hessian H using Eq. (25).

ii) Compute gradient $\vec{q}$ using Eq. (26).

iii) **For each triple** $\tau = (i, j, k) \in \Omega$.

1) $\vec{x}_p(\tau) \triangleq [x_{ip},\ x_{jp},\ x_{kp}]^T$, $\vec{x}_p^{(n)}(\tau) \triangleq [x_{ip}^{(n)},\ x_{jp}^{(n)},\ x_{kp}^{(n)}]^T$, form $H(\tau)$ and $\vec{q}(\tau)$ from elements in H and $\vec{q}$ with indexes corresponding to $\tau = (i, j, k)$, respectively.

2) Find and save the optimal $\hat{\vec{x}}_p(\tau)$ and the corresponding function value $\phi_p^{(n)}\left(\hat{\vec{x}}_p(\tau)\right)$ of the convex quadratic programming problem in Eq. (27) using GSMO.

End

iv) Determine the optimal triplet $\hat{\tau}$ by comparing all $\phi_p^{(n)}\left(\hat{\vec{x}}_p(\tau)\right)$, i.e.,

$$\hat{\tau} = \underset{\tau\in\Omega}{argmin}\ \phi_p^{(n)}\left(\hat{\vec{x}}_p(\tau)\right).$$

v) Obtain $\hat{\vec{x}}_p \equiv \hat{\vec{x}}_p(\hat{\tau})$ with padded zeros for $l \notin \tau$.

vi) Update all pixels $\vec{x}^{(n+1)} = (\hat{\vec{x}}_1, \ldots, \hat{\vec{x}}_p, \ldots, \hat{\vec{x}}_{N_p})$.

End

The stopping criterion is set as the difference between two adjacent iterations. The program stops when the difference between two adjacent iterations is less than a preset threshold.

Author Manuscript

This article is protected by copyright. All rights reserved

2.4. Data acquisition

The proposed method is evaluated using digital phantom, Catphan©600 phantom data and three sets of patient data. The linear attenuation coefficients in the digital phantom are obtained from the National Institute of Standards and Technology (NIST) database[31]. We generate DECT measurements at 75kVp and 140kVp spectra with 12mm Al filter, respectively. The high- and low-energy spectra of incident x-ray photons are simulated using Siemens simulator[32]. The source to detector distance is 1500 mm, and the source to rotation center distance is 1000 mm. The detector is composed of 1024×768 pixels with the physical size of 0.388×0.388 mm^2 per pixel. A total number of 676 projections over [0° 360°) are acquired. Poisson noise is added to the simulated projection data. The high- and low-energy CT images are reconstructed using the standard filtered back projection (FBP) algorithm[33, 34] with a dimension of 512×512 and a physical size of 0.5×0.5 mm^2 per pixel.

The Catphan©600 phantom data is acquired on a tabletop cone-beam CT (CBCT) system, whose geometry matches that of a Varian On-Board Imager (OBI) on the Trilogy radiation therapy machine. The CB4030 flat-panel detector (Varian Medical Systems) has 1024 × 768 pixels with a physical size of 0.388 mm × 0.388 mm per pixel. The scanned x-ray energies are 75 kVp and 125 kVp with a tube current of 80 mA and a pulse width of 13 ms. In each scan, a total number of 655 projections are acquired over [0° 360°). The projections with scatter contamination inherently suppressed is acquired using a fan-beam geometry with a longitudinal beam width of 15 mm on the detector.[35] The reconstructed images have a dimension of 512 × 512 with a size of 0.5 mm × 0.5 mm per pixel.

The patient data are scanned by Siemens SOMATOM Definition flash CT scanner and Siemens SOMATOM Force CT scanner using dual-energy CT imaging protocols. Both CT scanners apply the dual-source strategy for dual-energy data acquisition. The protocols of the patient data acquisition are listed in Table 2.

Table 2 Data acquisition parameters applied in patient data acquisition

Body part		pelvis	head	thigh
Scanner		Siemens SOMATOM Definition flash CT	Siemens SOMATOM Definition flash CT	Siemens SOMATOM Force CT
High-energy CT image	Peak voltage (kVp)	140	140	150
	X-ray Tube Current(mA)	146	364	97

This article is protected by copyright. All rights reserved

Author Manuscript

	Exposure Time(s)	0.500	0.285	0.500
	Current-exposure Time Product (mAs)	73.0	103.7	48.5
	noise STD(mm^{-1})	4.09e-04	1.57e-04	3.43e-04
	Helical Pitch	0.7	0.7	0.7
	Gantry Rotation Speed(circle/second)	0.28	0.28	0.25
Low-energy CT image	Peak voltage (kVp)	100	80	80
	X-ray Tube Current(mA)	186	648	148
	Exposure Time(s)	0.500	0.285	0.500
	Current-exposure Time Product (mAs)	93.0	184.7	74.0
	noise STD(mm^{-1})	7.27e-04	3.61e-04	4.48e-04
	Helical Pitch	0.7	0.7	0.7
	Gantry Rotation Speed(circle/second)	0.28	0.28	0.25

2.5. Evaluation

We compared the performance of the proposed method with those using the direct inversion[1, 2]. To further evaluate the performance of proposed method, we also apply a classical separate low-pass filtration method[36, 37] to suppress the high noise in the direct decomposition[1, 2].

The noise is quantitatively measured using STD of the image pixels within a uniform region of interest (ROI), and it is defined as

$$\mathrm{STD} = \sqrt{\frac{1}{M}\sum_{m=1}^{M}(x_{lm} - \overline{x}_l)^2}, \tag{28}$$

where m is the pixel index within the ROI, x_{lm} is the value of each pixel of the ROI for the l-th material image, $\overline{x}_l$ is the mean of the ROI for the material image, and M is the total number of pixels in the selected ROI.

The volume fraction accuracy of L_0 materials study is quantified as

$$VF = \left(1 - \frac{1}{L_0}\sum_{l=1}^{L_0}\frac{\|x_l{}^{truth} - \overline{x}_l\|}{x_l{}^{truth}}\right) \times 100\% \tag{29}$$

where $x_l{}^{truth}$ and $\overline{x}_l$ are the ground truth and decomposition result of the volume fraction for the l-th material image, respectively. L_0 is the total number of materials.

To investigate the image quality at the same noise level using different algorithms, a uniform area in the decomposed images is selected as the region of interest (ROI), and noise power spectrum (NPS) is applied as a metric to evaluate the image quality. The 2D NPS is defined as

$$NPS \approx |DFT_2\{f\}|^2 \tag{30}$$

This article is protected by copyright. All rights reserved

Author Manuscript

where f denotes the ROI in which gray values are offset to achieve a zero mean, $DFT_2\{f\}$ is the 2D Discrete Fourier Transform (DFT) on f. [38]

To evaluate the spatial resolution of decomposition results, the modulation transfer function (MTF)[39] is calculated on the digital and Catphan©600 phantoms. The MTF is obtained using the Fourier transform on the line spread function (LSF), which is the gradient of object edge profile. In addition, to minimize the fluctuation due to image noise, the resultant MTF is calculated from the average profile of adjacent boundaries of object. The measured frequencies at MTF magnitude decreased to 0.5 (-3dB) are compared to evaluate the relative spatial resolution[40].

In the Catphan©600 phantom study, the decomposition accuracy is further evaluated using the electron density. The electron density is calculated as[4]:

$$\vec{\rho}_e = \sum_{l=1}^{L_0} \rho_l \, \vec{x}_l. \tag{31}$$

where $\vec{x}_l$ and ρ_l are volume fraction and electron density of the *l*-th basis material, respectively. L_0 is the total number of materials. In each rod, the average percentage error of electron density is calculated as

$$E(\%) = \left(\frac{|\bar{\rho}_e - \rho_e^{truth}|}{\rho_e^{truth}} \right) \times 100\%. \tag{32}$$

where $\bar{\rho}_e$ is the average electron density inside one rod, ρ_e^{truth} is the ground truth of electron density in the corresponding rod. The root-mean-square percentage errors RMSE(%) of all the rods are summarized to quantify the decomposition accuracy of electron density.

3. Results

3.1 Digital phantom study

The digital phantom consists of four types of area as shown in Fig. 1(a). The background is fat and labeled as #1. The bone is labeled as #2, and the muscle is labeled as #3. To better evaluate the decomposition performance, mixed materials are included within one pixel and the area is labeled as #4. Area #4 consists of fat and muscle, and the proportion of fat to muscle is 3:7.

This article is protected by copyright. All rights reserved

Author Manuscript

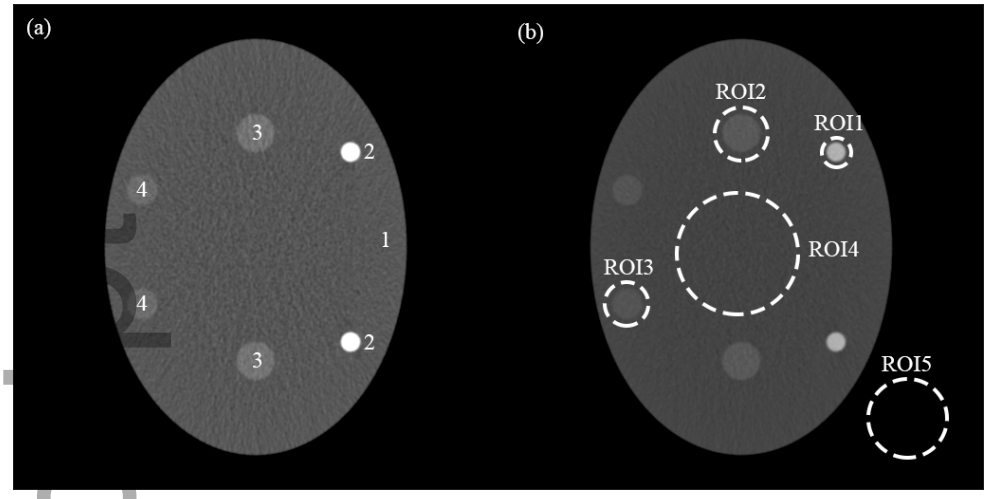

Fig. 1. CT images of the digital phantom: (a) The low-energy: 75kVp and (b) The high-energy: 140kVp. Display window is [0.01 0.04] mm^{-1}. The components of ROIs are bone (ROI1), muscle (ROI2), mixture (ROI3), fat (ROI4), and air (ROI5), respectively.

We select bone, fat, muscle and air as the basis materials. The decomposed basis material images are shown from the 1st to the 4th column in Fig. 2. The 1st row shows the results using direct inversion without noise suppression. The 2nd row shows the results using low-pass filtration method. The 3rd row shows the results using the proposed method. For fair comparison, the decomposition results of the low-pass filtration and the proposed methods are compared at the comparable noise STD. The proposed method successfully differentiates basis materials and suppresses the high noise STD in the direct decomposition results.

Author Manuscript

This article is protected by copyright. All rights reserved

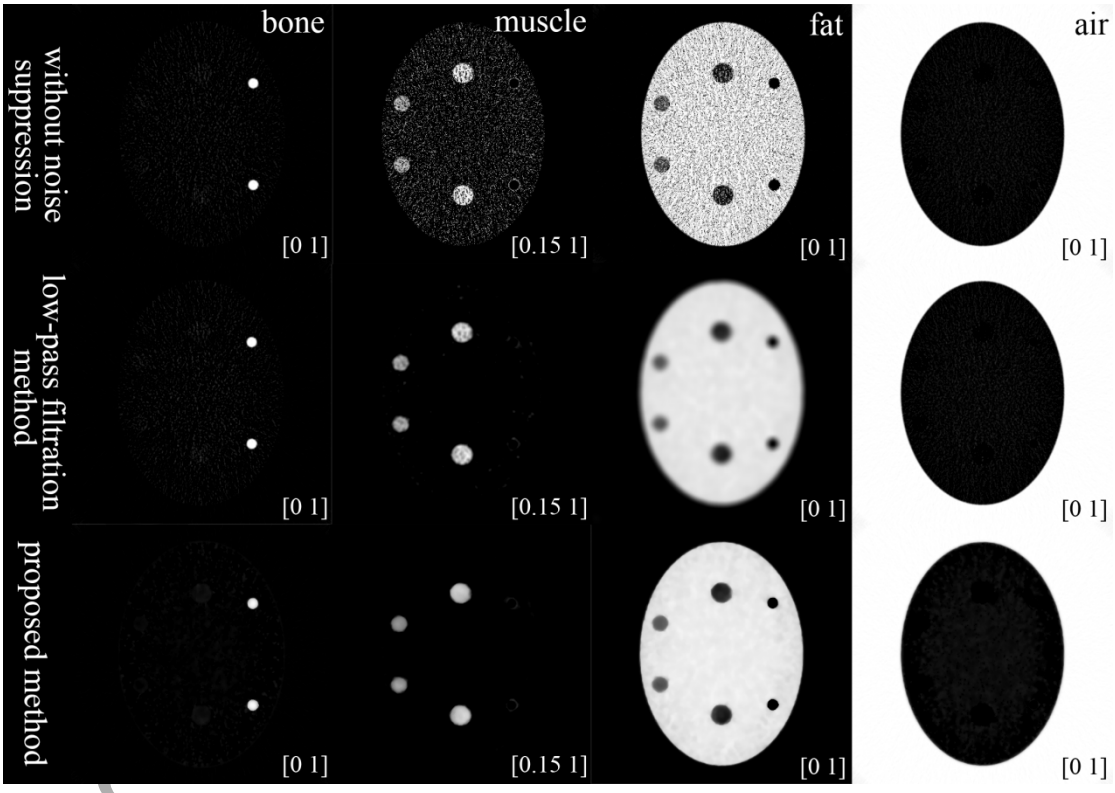

Fig. 2. The decomposed bone (the 1st column), muscle (the 2nd column), fat (the 3rd column) and air (the 4th column) images of the digital phantom. Display windows are shown in the bottom-right corner.

For quantitative analysis, several ROIs located within the uniform area of the basis materials are selected in the dashed circles of Fig. 1(b). The means and noise STDs of the decomposed basis material images are summarized in Table 3. The volume fraction accuracies are 82.42%, 92.43% and 93.77% using the direct inversion, the low-pass filtration and the proposed method, respectively. The proposed method improves the volume fraction accuracy by 11.35% compared with the direct inversion. In addition, the proposed method successfully differentiates the mixed materials within one pixel. In ROI3 where fat and muscle are mixed, the proposed method increases the volume fraction accuracy by 24.66% as compared with the direct inversion method.

Table 3. The means and STDs of decomposed images within each ROI

Methods	ROI1	ROI2	ROI3		ROI4	ROI5
	Bone	Muscle	Muscle	Fat	Fat	Air
Ground truth	1.000	1.000	0.700	0.300	1.000	1.000
W/o noise suppression	0.9760±0.0089	0.7282±0.2614	0.5366±0.2660	0.4047±0.2517	0.8262±0.2319	0.9970±0.0041
Low-pass filtration	0.9760±0.0089	0.7817±0.0839	0.6557±0.0405	0.3154±0.0053	0.9058±0.0091	0.9970±0.0041
Proposed method	0.9774±0.0040	0.8103±0.0239	0.6697±0.0104	0.3138±0.0050	0.9308±0.0084	0.9973±0.0036

This article is protected by copyright. All rights reserved

The image quality of the low-pass filtration is worse than that using the proposed method despite the comparable noise STD. The major reason is that noise correlation is included into the proposed scheme. To take a deep look into the frequency characteristics, the NPS is measured within an ROI of 200 by 200 pixels centered in the decomposed fat image, and the result is shown in Fig. 3. The low-pass filtration method removes the textures in the decomposed results due to its strong and uncorrelated noise suppression.

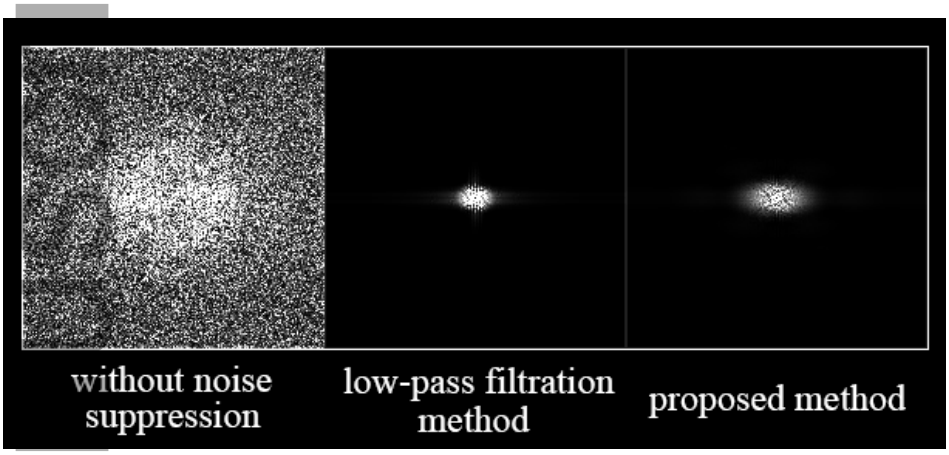

Fig. 3 Measured NPS on the decomposed fat image generated using different methods.

The display windows is [0 4000].

To evaluate the capability of spatial resolution maintenance, the typical MTFs of muscle and mixture are plotted in Fig. 4. Compared with the low-pass filtration method, the proposed method increases the spatial resolution by an overall factor of 1.64 at MTF magnitude decreased to 50%.

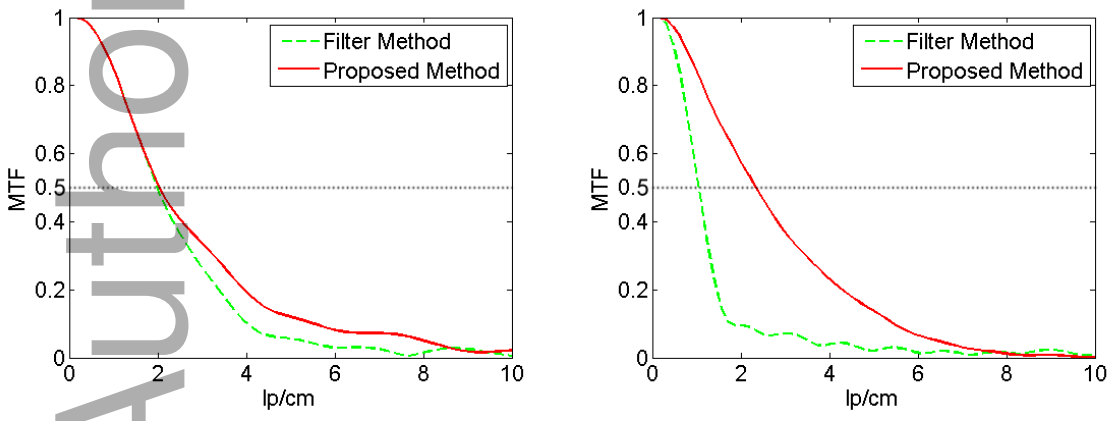

Fig. 4. MTF curves measured on the muscle and mixture areas

3.2 Catphan©600 phantom study

This article is protected by copyright. All rights reserved

The proposed method is evaluated using a contrast rod slice of the Catphan©600 phantom. The low- and high-energy CT images are shown in Fig. 5.

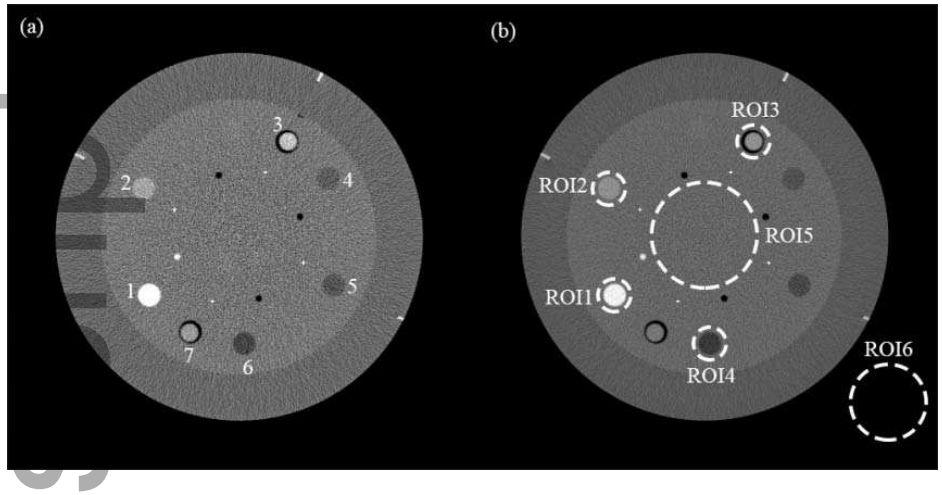

Fig. 5. CT images of the Catphan©600 phantom on the contrast rods slice: (a) The low-energy: 75kVp and (b) The high-energy: 125kVp. Display window is [0.01 0.04] mm^{-1}. The components of ROIs are Teflon (ROI1), Delrin (ROI2), Iodine solution of 10 mg/ml (ROI3), PMP (ROI4), Inner soft-tissue (ROI5) and Air (ROI6), respectively.

In this study, we insert iodine solutions with different concentrations into the phantom, whose nominal concentrations are 10 mg/ml and 5 mg/ml, respectively. The rods in this slice are labeled in Fig. 5(a): Teflon (labeled as #1), Delrin (labeled as #2), Iodine solution of 10 mg/ml (labeled as #3), Polystyrene (labeled as #4), low density Polyethylene (LDPE) (labeled as #5), Polymethylpentene (PMP) (labeled as #6), Iodine solution of 5 mg/ml (labeled as #7). We select Teflon (ROI1), Delrin (ROI2), Iodine solution of 10 mg/ml (ROI3), PMP (ROI4), Inner soft-tissue (ROI5) and Air (ROI6) as the basis materials. The decomposed basis material images are shown from the 1st to the 6th column in Fig. 6. The decomposition results using different methods are shown from the 1st to the 3rd row. The enlarged views of corresponding material images highlighted with white dashed boxes from the 1st to the 4th column are shown in the bottom-left corner. The proposed method successfully differentiates basis materials and suppresses the high noise STD in the direct decomposition. In addition, the iodine solution is infused into plastic bottles, whose linear attenuation coefficient is close to PMP. In the decomposed results, the proposed method still distinguishes them from those in the PMP image.

This article is protected by copyright. All rights reserved

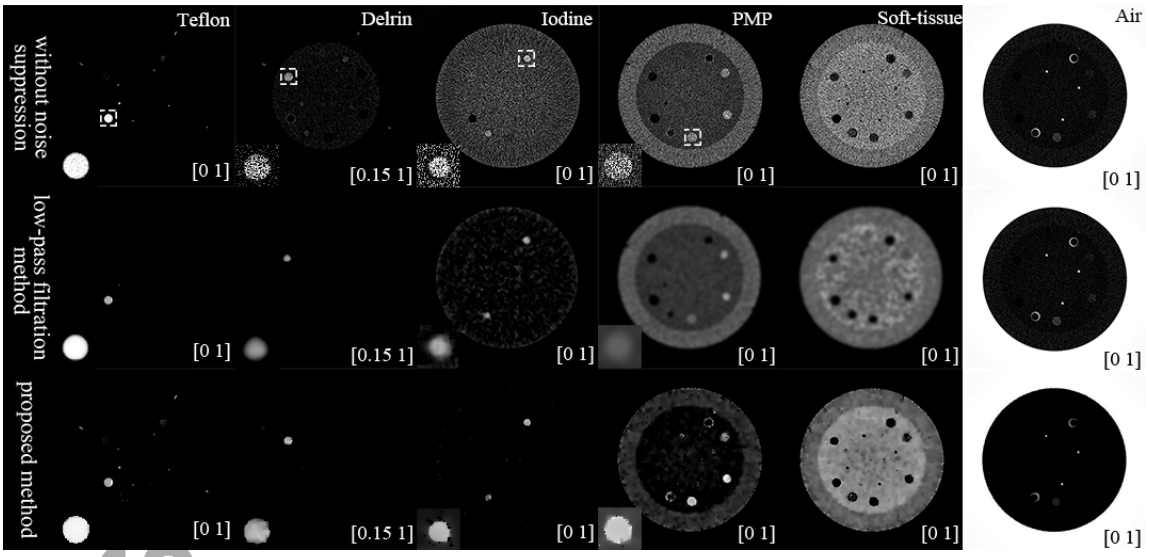

Fig. 6.The decomposed Teflon (the 1st column), Delran (the 2nd column), Iodine (the 3rd column), PMP (the 4th column), Soft-tissue (the 5th column) and Air (the 6th column) images of the Catphan©600 phantom on the contrast rods slice. The display windows are shown in the bottom-right corner of the subfigures.

For quantitative analysis, the means and noise STDs of the decomposed basis material images within the ROIs shown in Fig. 5 (b) are summarized in Table 4. The volume fraction accuracies using the three methods (direction inversion, low-pass filtration and the proposed) are 68.62%, 66.16% and 79.35%, respectively. The proposed method improves the volume fraction accuracy by 10.73% and 13.19% as compared with the direct inversion and low-pass filtration method, respectively.

Table 4 The means and STDs of decomposed images within each ROI

Methods	ROI1 Teflon	ROI2 Delran	ROI3 Iodine	ROI4 PMP	ROI5 Soft-tissue	ROI6 Air
W/o noise suppression	0.9578±0.0642	0.5852±0.3340	0.6190±0.3290	0.5067±0.3088	0.4493±0.3236	0.9995±0.0037
Low-pass filtration	0.9578±0.0642	0.6089±0.0504	0.6346±0.0475	0.3676±0.0078	0.4015±0.0398	0.9994±0.0023
Proposed method	0.9615±0.0043	0.7306±0.0367	0.7112±0.0188	0.7788±0.0071	0.5790±0.0388	0.9999±0.0018

The estimated average electron densities and the RMSE(%) for different contrast rod materials are summarized in Table 5. The RMSE(%) is 32.70% in the low-pass filtration method, and decreased to 11.81% in the proposed method. The proposed method achieves the balance between high image quality and strong noise suppression.

Table 5. Electron densities inside the Catphan©600 contrast rods. The numbers of the rods are marked in Fig. 5 (a). The last column is RMSE(%) of the seven rods. The electron density of iodine solutions is calculated based on iodine concentrations. The unit of the electron density is 10^{23} e/cm^3.

This article is protected by copyright. All rights reserved

Author Manus

Rods	1 Teflon	2 Delrin	3 Iodine solution (10 mg/ml)	4 Polystyrene	5 LDPE	6 PMP	7 Iodine solution (5 mg/ml)	RMSE(%)
Ground truth	6.240	4.525	3.368	3.400	3.155	2.851	3.356	
W/o noise suppression	6.158	4.127	3.882	2.984	2.729	2.274	3.370	
Average Percentage Errors E(%)	1.31%	8.80%	15.26%	12.24%	13.50%	20.24%	0.42%	12.27%
Low-pass filtration	5.999	3.318	3.025	2.716	1.809	1.232	2.190	
Average Percentage Errors E(%)	3.86%	26.67%	10.18%	20.12%	42.66%	56.79%	34.74%	32.70%
Proposed method	6.171	4.288	3.936	3.140	2.769	2.243	3.348	
Average Percentage Errors E(%)	1.11%	5.24%	16.86%	7.65%	12.23%	21.33%	0.24%	11.81%

To take a deep look into the frequency characteristics, the NPS is measured within an ROI of 160 by 160 pixels centered in the decomposed soft-tissue image, and the result is shown in Fig. 7. The low-pass filtration method removes the texture of decomposed results with strong noise suppression.

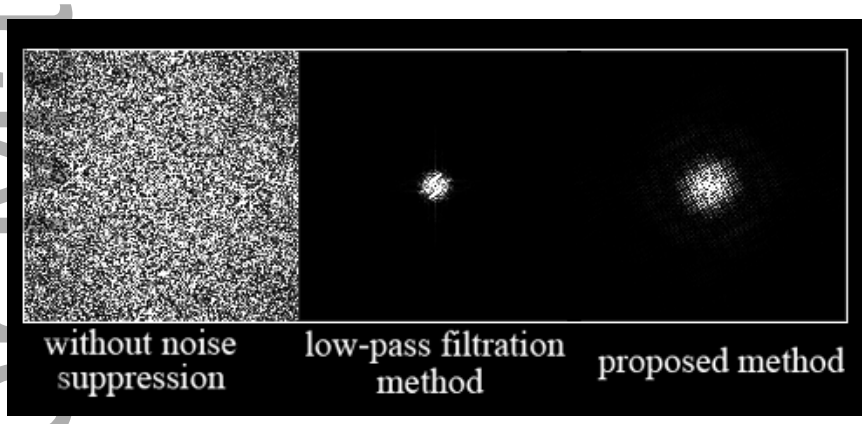

Fig. 7. Measured NPS on the decomposed soft-tissue image generated using different methods. The display windows: [0 4000]

To evaluate the capability of spatial resolution retaining, the typical MTFs of iodine solution (10 mg/ml) and PMP are plotted in Fig. 8. Compared with the low-pass filtration method, the proposed method increases spatial resolution by an overall factor of 2.16 at MTF magnitude decreased to 50%.

Author Manuscript

This article is protected by copyright. All rights reserved

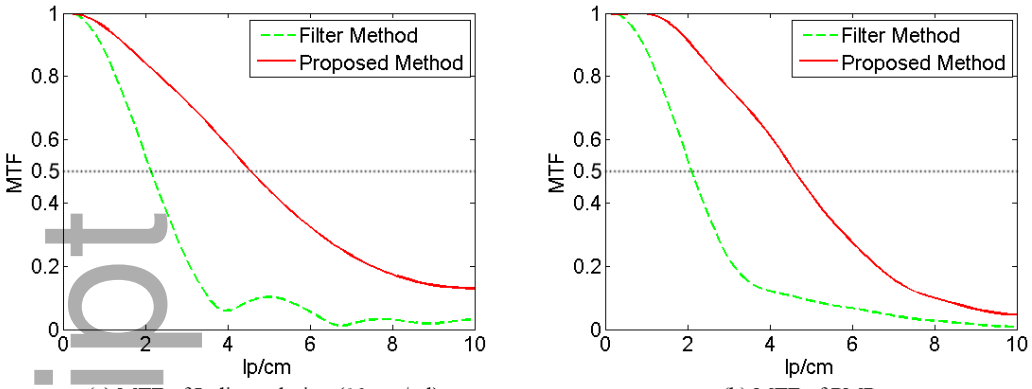

(a) MTF of Iodine solution (10 mg/ml) (b) MTF of PMP

Fig. 8. MTF curves measured on iodine solution (10 mg/ml) and PMP areas

3.3 Patient Studies

The proposed method is also evaluated using the clinical data.

3.3.1 Pelvis study

The CT images of pelvis patient are shown in Fig. 9 .

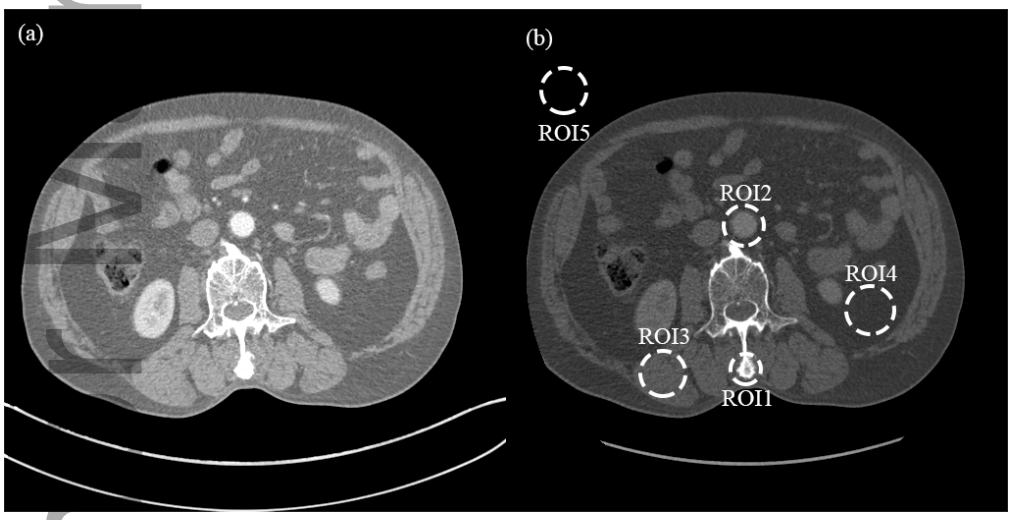

Fig. 9. CT images of a pelvis patient. (a) The low-energy: 100kVp and (b) The high-energy: 140kVp. Display window is [0.012 0.032] mm^{-1}. The major components of ROIs are bone (ROI1), iodine solution (ROI2), muscle (ROI3), fat (ROI4), and air (ROI5), respectively.

The bone, iodine, muscle, fat and air are selected as the basis materials. And the decomposed basis material images are shown from the 1st to the 5th column in Fig. 10. The decomposition results using different methods are shown from the 1st to the 3rd row. The proposed method successfully differentiates basis materials and suppresses the high noise STD in the direct decomposition.

This article is protected by copyright. All rights reserved

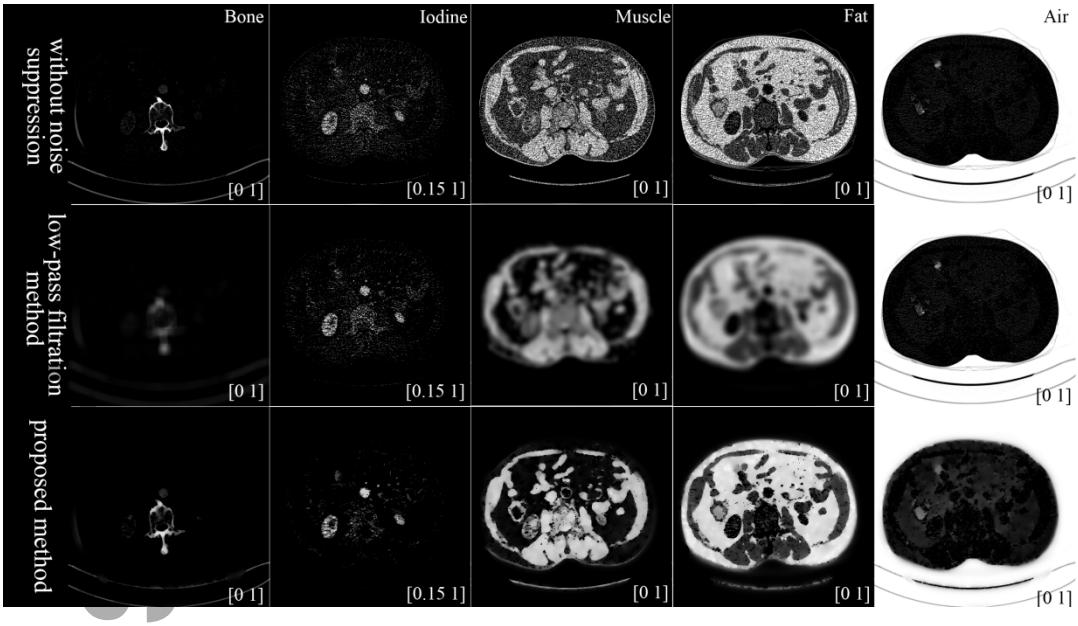

Fig. 10. The decomposed bone (the 1st column), iodine (the 2nd column), muscle (the 3rd column), fat (the 4th column), and air (the 5th column) images. The display windows are shown in the bottom-right corner.

For quantitative analysis, the means and noise STDs in the ROIs of the decomposed basis material images shown in Fig. 9 (b) are summarized in Table 6. The volume fraction accuracies using the three methods (direction inversion, low-pass filtration and the proposed) are 77.59%, 72.06% and 86.29%, respectively. The proposed method improves the volume fraction accuracy by 8.70% and 14.23% compared with the direct inversion and low-pass filtration method, respectively.

Table 6. The means and STDs of decomposed images within each ROI

Methods	ROI1 Bone	ROI2 Iodine	ROI3 Muscle	ROI4 Fat	ROI5 Air
W/o noise suppression	0.8652±0.1248	0.6282±0.2781	0.6623±0.2603	0.7237±0.2711	1.0000±0.0000
Low-pass filtration	0.4916±0.0159	0.6524±0.1867	0.6888±0.0272	0.7703±0.0225	1.0000±0.0000
Proposed method	0.8806±0.0056	0.7801±0.1681	0.7914±0.0194	0.8623±0.0208	1.0000±0.0000

The NPS is measured within an ROI of 100 by 100 pixels in the decomposed fat image, and the result is shown in Fig. 11. The low-pass filtration method removes the texture of decomposed results with strong noise suppression, while the proposed method still retains the texture information due to the correlated noise suppression scheme.

This article is protected by copyright. All rights reserved

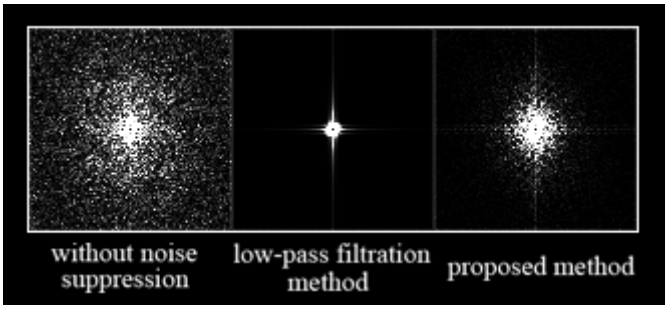

Fig. 11. Measured NPS on the decomposed fat image generated using different methods.

The display windows: [0 2500]

3.3.2 Head study

The CT images of head patient are shown in Fig. 12.

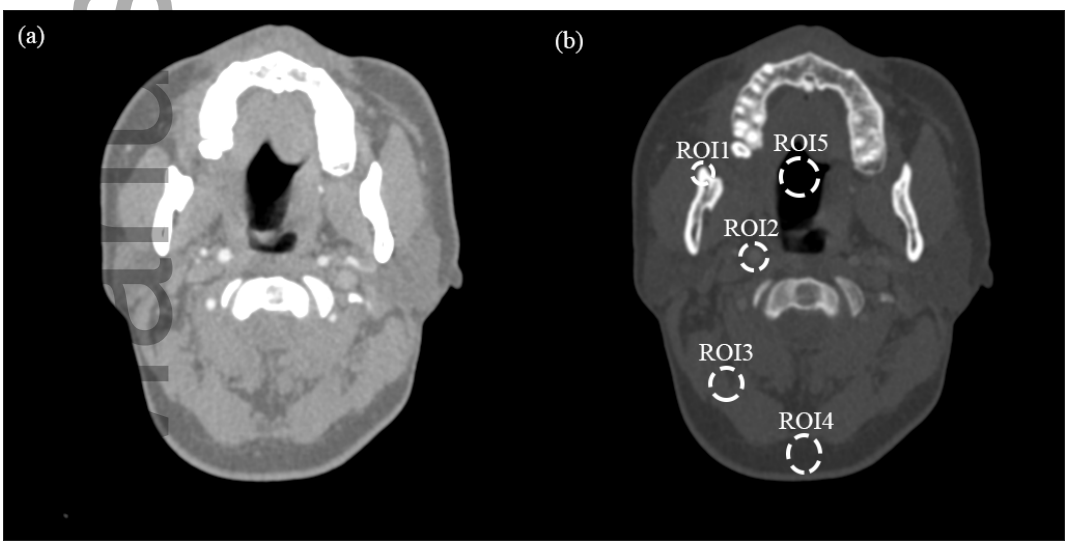

Fig. 12. CT images of a head patient. (a) The low-energy: 80kVp and (b) The high-energy: 140kVp. Display window is [0.01 0.035] mm^{-1}. The major components of ROIs are bone (ROI1), iodine solution (ROI2), muscle (ROI3), fat (ROI4), and air (ROI5), respectively.

The bone, iodine, muscle, fat and air are selected as the basis materials. And the decomposed basis material images are shown in Fig. 13. The proposed method successfully differentiates basis materials and suppresses the high noise STD in the direct decomposition. In addition, the areas pointed by the red arrows are parotid glands, whose linear attenuation coefficient is between fat and muscle. In Fig. 13, the proposed method successfully differentiates these areas, while retaining the spatial resolution of decomposition results.

This article is protected by copyright. All rights reserved

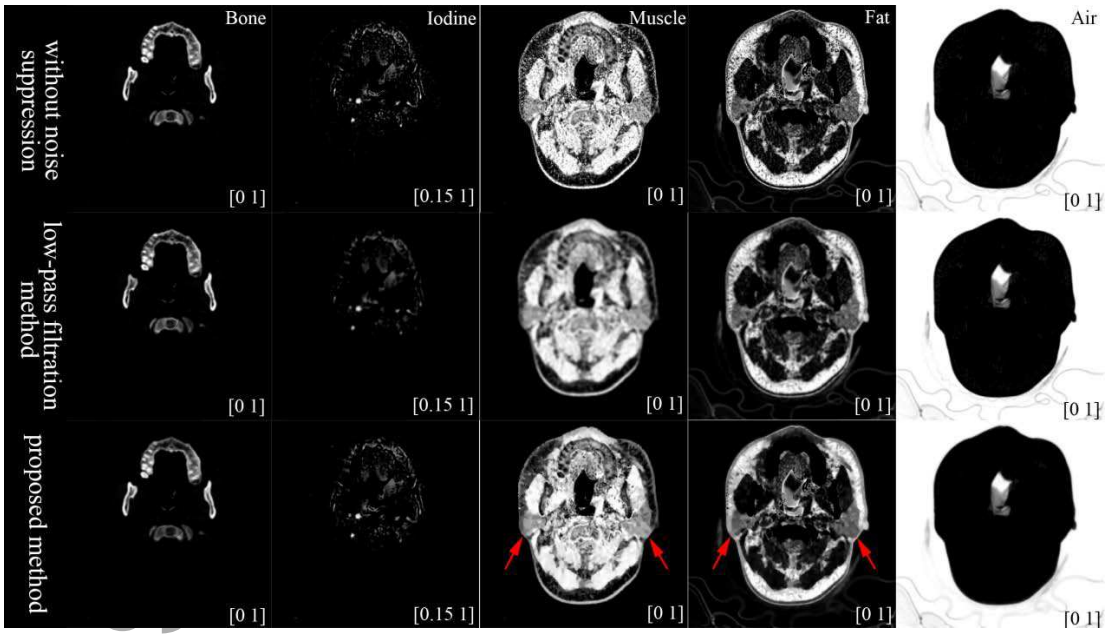

Fig. 13. The decomposed bone (the 1st column), iodine (the 2nd column), muscle (the 3rd column), fat (the 4th column), and air (the 5th column) images. The display windows are shown in the bottom-right corner.

For quantitative analysis, the means and noise STDs of the decomposed basis material images within the ROIs shown in Fig. 12 (b) are summarized in Table 7. The volume fraction accuracies using the three methods (direction inversion, low-pass filtration and the proposed) are 92.99%, 92.80% and 94.13%, respectively.

Table 7. The means and STDs of decomposed images within each ROI

Methods	ROI1 Bone	ROI2 Iodine	ROI3 Muscle	ROI4 Fat	ROI5 Air
W/o noise suppression	0.9719±0.0556	0.9056±0.0656	0.9382±0.0733	0.8602±0.1465	0.9735±0.0226
Low-pass filtration	0.9713±0.0554	0.8700±0.0572	0.9573±0.0210	0.8679±0.0863	0.9735±0.0226
Proposed method	0.9722±0.0524	0.9135±0.0540	0.9575±0.0161	0.8898±0.0843	0.9737±0.0222

3.3.3 Thigh study

The CT images of thigh patient are shown in Fig. 14.

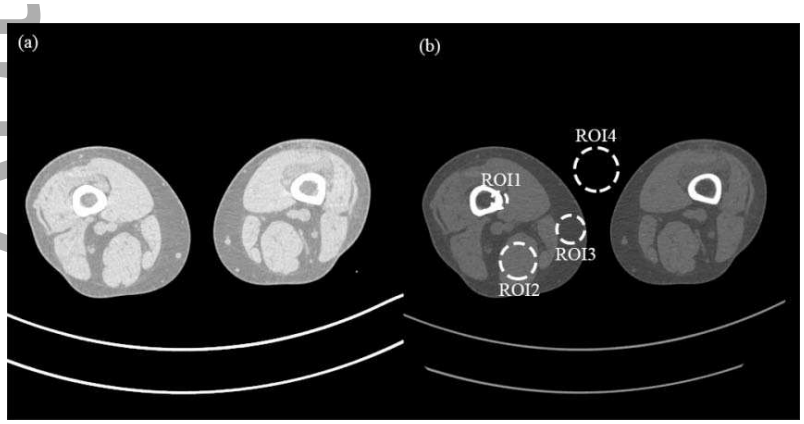

Fig. 14. CT images of a thigh patient. (a) The low-energy: 80kVp and (b) The high-energy: 150kVp. Display

This article is protected by copyright. All rights reserved

window is [0.012 0.032] mm^{-1}. The major components of ROIs are bone (ROI1), muscle (ROI2), fat (ROI3), and air (ROI4), respectively.

The bone, muscle, fat and air are selected as the basis materials. And the decomposed basis material images are shown in Fig. 15. The proposed method successfully differentiates basis materials and suppresses the high noise STD in the direct decomposition. In addition, the areas pointed by the red arrows are bone marrow and connective fiber, whose linear attenuation coefficients are between those of fat and muscle. In Fig. 15, the proposed method successfully differentiates these areas, while retaining the spatial resolution of decomposition results.

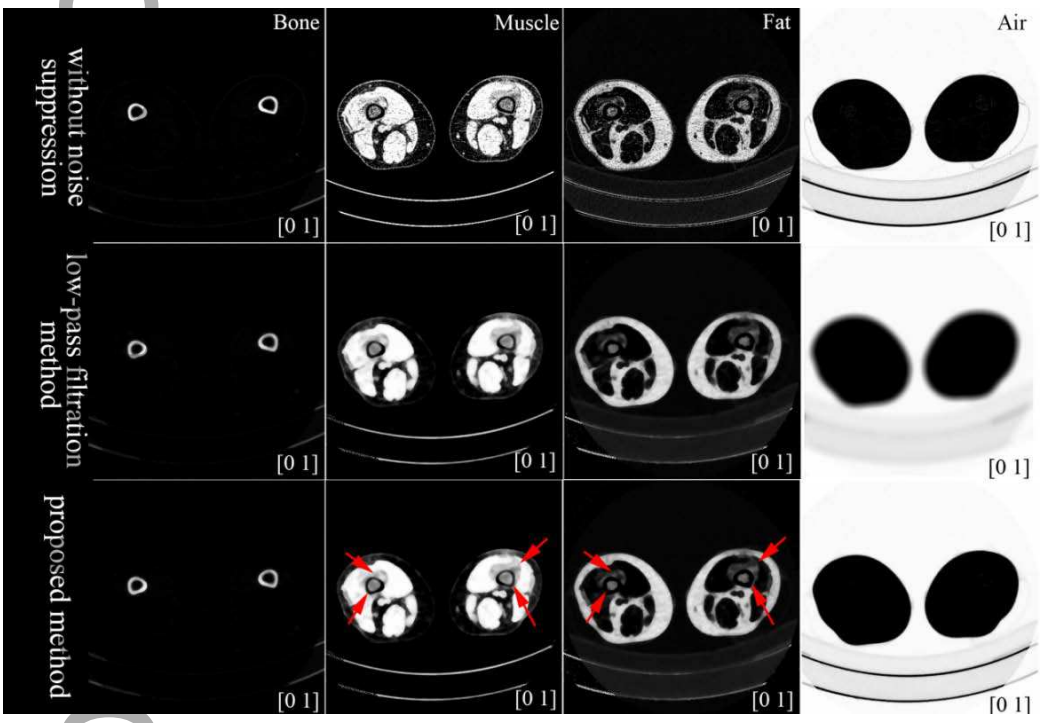

Fig. 15. The decomposed bone (the 1st column), muscle (the 2nd column), fat (the 3rd column), and air (the 4th column) images. The display windows are shown in the bottom-right corner.

For quantitative analysis, the means and noise STDs of the decomposed basis material images within the ROIs shown in Fig. 14 (b) are summarized in Table 8. The volume fraction accuracies using the three methods (direction inversion, low-pass filtration and the proposed) are 91.09%, 92.80% and 93.44%, respectively.

Table 8. The means and STDs of decomposed images within each ROI

Methods	ROI1 Bone	ROI2 Muscle	ROI3 Fat	ROI4 Air
W/o noise suppression	0.9099±0.0820	0.9451±0.1189	0.8086±0.1496	0.9801±0.0091
Low-pass filtration	0.9091±0.0379	0.9804±0.0229	0.8427±0.0400	0.9799±0.0021
Proposed method	0.9270±0.0353	0.9844±0.0199	0.8455±0.0311	0.9806±0.0020

This article is protected by copyright. All rights reserved

3.4. Implementation details

In the implementations, we initialized the proposed method using results of the direct inversion method. And the statistical weight V_p is normalized as $V_p = diag\left(var\left(\mu_{Hp}\right)/var\left(\mu_{Lp}\right),\ 1\right)$. The threshold of stopping criterion is set as 1.0e-05. The cost function of the proposed method has two tunable parameters. The parameter beta controls the noise-resolution, while delta controls the edge preservation. For different materials, the decomposed image contains different content and the situations of neighbored pixels are also different. Therefore, we empirically selected the optimal combination of these parameters to balance the noise suppression and spatial resolution maintenance. Table 9 listed the regularization coefficients β_l, and the edge-preserving parameters δ_l for each material in every study.

Table 9. The regularization coefficients and edge-preserving parameters for each study

Data	β_l	δ_l
Digital phantom (for bone, muscle, fat and air images)	0.01, 0.01, 0.1, 0.01	0.1, 0.1, 0.01, 0.1
Catphan©600 phantom (for teflon, delrin, iodine, PMP, soft-tissue and air images)	0.6, 5, 2.5, 1, 1, 7	0.005, 0.005, 0.02, 0.012, 0.012, 0.012
pelvis patient data (for bone, iodine, muscle, fat and air images)	1, 1.5, 0.9, 0.9, 0.1	0.01, 0.005, 0.01, 0.01, 0.1
head patient data (for bone, iodine, muscle, fat and air images)	0.2, 0.3, 0.09, 0.09, 0.04	0.01, 0.005, 0.01, 0.01, 0.1
thigh patient data (for bone, muscle, fat and air images)	0.03, 0.01, 0.05, 0.09	0.05, 0.08, 0.01, 0.01

4. Discussion

We proposed a statistical image-domain MMD method for DECT. As in pervious work,[1-3] we applied mass and volume conservation constraints and the assumptions that each pixel contains at most three materials and material triplets vary among pixels to decrease the degrees of freedom to two per pixel for a given triplet so that reconstructing multiple-material images from DECT measurement is feasible. The cost function is in the form of PWLS reconstruction with a negative

This article is protected by copyright. All rights reserved

Author Manuscript

log-likelihood term and edge-preserving regularization for each material image. The statistical weight is determined by a data-based method accounting for the noise variance of high- and low-energy CT images. We applied the optimization transfer principles to design a series of pixel-wise separable quadratic surrogates (PWSQS) functions which monotonically decrease the cost function.[3] As the surrogates are pixel-wise separable, the proposed method can update all pixels simultaneously, which allows faster convergence. Since the cost function in Eq. (12) under constraints in Eqs. (2)-(4) is nonconvex, a good initialization is important to guarantee convergence to a decent local minimum. We initialized the proposed method using results of the direct inversion method. The proposed method is a practical image-domain method where CT images at low and high energies are modeled as weighted linear combinations of linear attenuation coefficients of basis materials with weights beginning their volume fractions. The proposed method incorporates noise variance of DECT images into statistical weight in PWLS estimation, which effectively overcomes the issue of magnified noise in the decomposed basis materials by the direct inversion method[1, 2].

The cost function of the proposed method has two tunable parameters (i.e., regularization coefficient and edge-preserving coefficient). The choice of parameters for one basis material image influences the decomposed images of other components. An appropriate combination of parameters needs to be carefully determined for each application. We empirically selected the optimal combination of these parameters to balance the noise suppression and spatial resolution maintenance. Determining tunable parameters remains a challenge for the proposed method, just as that for other methods with multiple parameters. In the future, we will further investigate optimal selection of these parameters using material-cross penalty, such as total nuclear variation (TNV)[41].

In the current implementation, we assumed uniform distribution of noise variance map in DECT images, and measured the noise variance inside a manually selected region of homogeneous material. The performance of the proposed method can be further improved by substituting the uniform noise variance map with a pixel-dependent one. Several analytic algorithms are proposed in literature to calculate the noise variance for DECT images. Wunderlich and Noo presented a method for computing image variance[42]. Li *et al.* proposed a computationally efficient technique for noise estimation directly from CT images[43]. A forward projection, based on

This article is protected by copyright. All rights reserved

Author Manuscript

a 2D fan-beam approximation, was used to generate the projection data, with a noise model incorporating the effects of the bowtie filter and automatic exposure control. The noise propagation from projection data to images was analytically derived. In future work, we will combine noise variance estimation with the proposed decomposition method, and evaluate its performance on clinical applications. In addition, we will do more studies on the clinical data to fully evaluate the efficacy of the proposed method.

5. Conclusions

We proposed a statistical image-domain MMD method using DECT measurements. The proposed method applies extra constraints of volume and mass conservation and the assumptions that at most three materials in each pixel and various material types among pixels. The proposed multi-material images are faithfully decomposed from the dual-energy measurements. It is thus practical to be implemented in clinical applications.

Acknowledgments

The work was supported by the Zhejiang Provincial Natural Science Foundation of China (Grant No. LR16F010001), National High-tech R&D Program for Young Scientists by the Ministry of Science and Technology of China (863 Program, 2015AA020917), Natural Science Foundation of China (NSFC Grant No. 81201091, 51305257), National Key Research Plan by the Ministry of Science and Technology of China (Grant No. 2016YFC0104507) and Key Laboratory of Diagnosis and Treatment of Neonatal Diseases of Zhejiang Province (2016-ZJKD-ND-004). Yong Long was partially supported by NSFC (61501292), Shanghai Pujiang Talent Program (15PJ1403900), SJTU-UM Collaborative Research Program and Returned Overseas Chinese Scholars Program. Yu Kuang was supported in part by an NIH/NIGMS grant (P20GM103440).

References

[1] R. Bhotika, B. Thomsen, "Multi-material decomposition of spectral CT images," Proceedings of SPIE - The International Society for Optical Engineering **7622**, 640–643 (2010).

[2] P.R. Mendonca, P. Lamb, D.V. Sahani, "A Flexible Method for Multi-Material Decomposition

This article is protected by copyright. All rights reserved

Author Manuscript

of Dual-Energy CT Images," IEEE Transactions on Medical Imaging **33**, 99-116 (2014).

[3] Y. Long, J.A. Fessler, "Multi-material decomposition using statistical image reconstruction for spectral CT," IEEE Transactions on Medical Imaging **33**, 1614-1626 (2014).

[4] T. Niu, X. Dong, M. Petrongolo, L. Zhu, "Iterative image-domain decomposition for dual-energy CT," Medical Physics **41**, 041901 (2014).

[5] R.E. Alvarez, A. Macovski, "Energy-selective reconstructions in X-ray computerized tomography," Physics in Medicine & Biology **21**, 733-744 (1976).

[6] R.E. Alvarez, A. Macovski, "X-ray spectral decomposition imaging system," (US, 1977).

[7] A. Macovski, R.E. Alvarez, J.L. Chan, J.P. Stonestrom, L.M. Zatz, "Energy dependent reconstruction in X-ray computerized tomography," Computers in Biology & Medicine **6**, 325-336 (1976).

[8] M.W. Jr, R.E. Alvarez, A. Macovski, "Initial results with prereconstruction dual-energy computed tomography (PREDECT)," Radiology **140**, 421-430 (1981).

[9] J.P. Stonestrom, R.E. Alvarez, A. Macovski, "A framework for spectral artifact corrections in x-ray CT," IEEE Transactions on Biomedical Engineering **28**, 128-141 (1981).

[10] A.D. Laidevant, S. Malkov, C.I. Flowers, K. Kerlikowske, J.A. Shepherd, "Compositional breast imaging using a dual-energy mammography protocol," Medical Physics **37**, 164-174 (2010).

[11] X. Liu, L. Yu, A.N. Primak, C.H. Mccollough, "Quantitative imaging of element composition and mass fraction using dual-energy CT: three-material decomposition. Med Phys," Medical Physics **36**, 1602-1609 (2009).

[12] W. Huh, J.A. Fessler, "Model-based image reconstruction for dual-energy X-ray CT with fast KVP switching," Proceedings, 326-329 (2009).

[13] T. Johnson, C. Fink, S.O. Schönberg, M.F. Reiser, "Dual Energy CT in Clinical Practice," Medical Physics **38**, 6346-6346 (2011).

[14] C.H. Mccollough, A.N. Primak, O. Saba, H. Bruder, K. Stierstorfer, R. Raupach, C. Suess, B. Schmidt, B.M. Ohnesorge, T.G. Flohr, "Dose performance of a 64-channel dual-source CT scanner," Radiology **243**, 775-784 (2007).

[15] M. Petersilka, H. Bruder, B. Krauss, K. Stierstorfer, T.G. Flohr, "Technical principles of dual source CT," European Journal of Radiology **68**, 362-368 (2008).

This article is protected by copyright. All rights reserved

Author Manuscript

[16] M. Rafecas, G. Boning, B.J. Pichler, E. Lorenz, "A Monte Carlo study of high-resolution PET with granulated dual-layer detectors," Nuclear Science IEEE Transactions on **48**, 1490-1495 (2001).

[17] B.R. Foygel, E.Y. Sidky, S.T. Gilat, X. Pan, "An algorithm for constrained one-step inversion of spectral CT data," Physics in Medicine & Biology **61**, 3784-3818 (2015).

[18] E.Y. Sidky, Y. Zou, X. Pan, "Impact of polychromatic x-ray sources on helical, cone-beam computed tomography and dual-energy methods," Physics in Medicine & Biology **49**, 2293-2303 (2004).

[19] J. Harms, T. Wang, M. Petrongolo, T. Niu, L. Zhu, "Noise suppression for dual-energy CT via penalized weighted least-square optimization with similarity-based regularization," Medical Physics **43**, 2676-2686 (2016).

[20] M. Petrongolo, X. Dong, L. Zhu, "A general framework of noise suppression in material decomposition for dual-energy CT," Medical Physics **42**2015).

[21] R. Zhang, J.B. Thibault, C. Bouman, K. Sauer, J. Hsieh, "Model-Based Iterative Reconstruction for Dual-Energy X-Ray CT Using a Joint Quadratic Likelihood Model," IEEE Transactions on Medical Imaging **33**, 117-134 (2013).

[22] J.A. Fessler, W.L. Rogers, presented at the Biomedical Imaging, 2002. 5th IEEE EMBS International Summer School on2002 (unpublished).

[23] A.R. De Pierro, "A modified expectation maximization algorithm for penalized likelihood estimation in emission tomography," IEEE Transactions on Medical Imaging **14**, 132-137 (1995).

[24] H. Erdoğan, J.A. Fessler, "Monotonic algorithms for transmission tomography," IEEE Transactions on Medical Imaging **18**, 801-814 (1999).

[25] M.W. Jacobson, J.A. Fessler, "An expanded theoretical treatment of iteration-dependent majorize-minimize algorithms," IEEE Transactions on Image Processing **16**, 2411-2422 (2007).

[26] Y. Iijima, M. Murakawa, Y. Kasai, E. Takahashi, T. Higuchi, "Optimization Transfer Using Surrogate Objective Functions," Journal of Computational & Graphical Statistics **9**, 1-20 (2012).

[27] H. Erdogan, J.A. Fessler, "Ordered subsets algorithms for transmission tomography," Physics

This article is protected by copyright. All rights reserved

Author Manuscript

in Medicine & Biology **44**, 2835-2851 (1999).

[28] J.A. Fessler, presented at the Handbook of Medical Imaging, Volume 2. Medical Image Processing and Analysis2000 (unpublished).

[29] P.J. Huber, *Robust Statistics*. (Springer Berlin Heidelberg, 2011).

[30] S.S. Keerthi, E.G. Gilbert, "Convergence of a Generalized SMO Algorithm for SVM Classifier Design," Machine Learning **46**, 351-360 (2002).

[31] NIST, "X-Ray Mass Attenuation Coefficients," (https://www.nist.gov/pml/x-ray-mass-attenuation-coefficients).

[32] Siemens, (https://bps-healthcare.siemens.com/cv_oem/radIn.asp).

[33] A.C. Kak, M. Slaney, *Principles of computerized tomographic imaging*. (Society for Industrial and Applied Mathematics, 2001).

[34] F. Natterer, *The mathematics of computerized tomography*. (B. G. Teubner, 2001).

[35] T. Niu, M. Sun, J. Starlack, H. Gao, Q. Fan, L. Zhu, "Shading correction for on-board cone-beam CT in radiation therapy using planning MDCT images," Medical Physics **37**, 5395-5406 (2010).

[36] P.C. Johns, M.J. Yaffe, "Theoretical optimization of dual‐energy x‐ray imaging with application to mammography," Medical Physics **12**, 289-296 (1985).

[37] R.A. Rutherford, B.R. Pullan, I. Isherwood, "X-ray energies for effective atomic number determination," Neuroradiology **11**, 23-28 (1976).

[38] M. Petrongolo, L. Zhu, "Noise Suppression for Dual-Energy CT through Entropy Minimization," IEEE Transactions on Medical Imaging **34**, 2646-2646 (2015).

[39] S. Richard, D.B. Husarik, G. Yadava, S.N. Murphy, E. Samei, "Towards task-based assessment of CT performance: system and object MTF across different reconstruction algorithms," Medical Physics **39**, 4115-4122 (2012).

[40] E. Samei, M.J. Flynn, D.A. Reimann, "A method for measuring the presampled MTF of digital radiographic systems using an edge test device," Medical Physics **25**, 102-113 (1998).

[41] D.S. Rigie, P.J. La Rivière, "Joint reconstruction of multi-channel, spectral CT data via constrained total nuclear variation minimization," Physics in Medicine & Biology **60**, 1741-1762 (2015).

[42] A. Wunderlich, F. Noo, "Image covariance and lesion detectability in direct fan-beam x-ray

This article is protected by copyright. All rights reserved

Author Manuscript

computed tomography," Physics in Medicine & Biology **53**, 2471-2493 (2008).

[43] Z. Li, L. Yu, J.D. Trzasko, D.S. Lake, D.J. Blezek, J.G. Fletcher, C.H. McCollough, A. Manduca, "Adaptive nonlocal means filtering based on local noise level for CT denoising," Medical Physics **41**, 011908-011908 (2014).

Author Manuscript

This article is protected by copyright. All rights reserved

Table 1. Pseudocode of the pixel-wise separable quadratic surrogate (PWSQS) algorithm

I) Initialize $\vec{x}^{(0)}$ using the results of the direct inversion method.[1,2]

II) **For each iteration** n = 1,…, Niter

i) Compute Hessian *H* using Eq. (25).

ii) Compute gradient $\vec{q}$ using Eq. (26).

iii) **For each triple** $\tau = (i, j, k) \in \Omega$.

1) $\vec{x}_p(\tau) \triangleq [x_{ip,}\ x_{jp,}\ x_{kp}]^T$, $\vec{x}_p^{(n)}(\tau) \triangleq [x_{ip}^{(n)},\ x_{jp}^{(n)},\ x_{kp}^{(n)}]^T$, form $H(\tau)$ and $\vec{q}(\tau)$ from elements in *H* and $\vec{q}$ with indexes corresponding to $\tau = (i, j, k)$, respectively.

2) Find and save the optimal $\hat{\vec{x}}_p(\tau)$ and the corresponding function value $\phi_p^{(n)}\big(\hat{\vec{x}}_p(\tau)\big)$ of the convex quadratic programming problem in Eq. (27) using GSMO.

End

iv) Determine the optimal triplet $\hat{\tau}$ by comparing all $\phi_p^{(n)}\big(\hat{\vec{x}}_p(\tau)\big)$, i.e.,

$$\hat{\tau} = \underset{\tau\in\Omega}{argmin}\ \phi_p^{(n)}\big(\hat{\vec{x}}_p(\tau)\big).$$

v) Obtain $\hat{\vec{x}}_p \equiv \hat{\vec{x}}_p(\hat{\tau})$ with padded zeros for $l \notin \tau$.

vi) Update all pixels $\vec{x}^{(n+1)} = (\hat{\vec{x}}_1, \dots, \hat{\vec{x}}_p, \dots, \hat{\vec{x}}_{N_p})$.

End

Author Manuscript

This article is protected by copyright. All rights reserved

Table 2 Data acquisition parameters applied in patient data acquisition

Body part		pelvis	head	thigh
Scanner		Siemens SOMATOM Definition flash CT	Siemens SOMATOM Definition flash CT	Siemens SOMATOM Force CT
High-energy CT image	Peak voltage (kVp)	140	140	150
	X-ray Tube Current(mA)	146	364	97
	Exposure Time(s)	0.500	0.285	0.500
	Current-exposure Time Product (mAs)	73.0	103.7	48.5
	noise STD(mm^{-1})	4.09e-04	1.57e-04	3.43e-04
	Helical Pitch	0.7	0.7	0.7
	Gantry Rotation Speed(circle/second)	0.28	0.28	0.25
Low-energy CT image	Peak voltage (kVp)	100	80	80
	X-ray Tube Current(mA)	186	648	148
	Exposure Time(s)	0.500	0.285	0.500
	Current-exposure Time Product (mAs)	93.0	184.7	74.0
	noise STD(mm^{-1})	7.27e-04	3.61e-04	4.48e-04
	Helical Pitch	0.7	0.7	0.7
	Gantry Rotation Speed(circle/second)	0.28	0.28	0.25

Author Manuscript

This article is protected by copyright. All rights reserved

Table 3. The means and STDs of decomposed images within each ROI

Methods	ROI1	ROI2	ROI3		ROI4	ROI5
	Bone	Muscle	Muscle	Fat	Fat	Air
Ground truth	1.000	1.000	0.700	0.300	1.000	1.000
W/o noise suppression	0.9760±0.0089	0.7282±0.2614	0.5366±0.2660	0.4047±0.2517	0.8262±0.2319	0.9970±0.0041
Low-pass filtration	0.9760±0.0089	0.7817±0.0839	0.6557±0.0405	0.3154±0.0053	0.9058±0.0091	0.9970±0.0041
Proposed method	0.9774±0.0040	0.8103±0.0239	0.6697±0.0104	0.3138±0.0050	0.9308±0.0084	0.9973±0.0036

Author Manuscript

This article is protected by copyright. All rights reserved

Table 4 The means and STDs of decomposed images within each ROI

Methods	ROI1 Teflon	ROI2 Delran	ROI3 Iodine	ROI4 PMP	ROI5 Soft-tissue	ROI6 Air
W/o noise suppression	0.9578±0.0642	0.5852±0.3340	0.6190±0.3290	0.5067±0.3088	0.4493±0.3236	0.9995±0.0037
Low-pass filtration	0.9578±0.0642	0.6089±0.0504	0.6346±0.0475	0.3676±0.0078	0.4015±0.0398	0.9994±0.0023
Proposed method	0.9615±0.0043	0.7306±0.0367	0.7112±0.0188	0.7788±0.0071	0.5790±0.0388	0.9999±0.0018

Author Manuscript

This article is protected by copyright. All rights reserved

Table 5. Electron densities inside the Catphan©600 contrast rods. The numbers of the rods are marked in Fig. 5 (a). The last column is RMSE(%) of the seven rods. The electron density of iodine solutions is calculated based on iodine concentrations. The unit of the electron density is 10^{23} e/cm^3.

Rods	1 Teflon	2 Delrin	3 Iodine solution (10 mg/ml)	4 Polystyrene	5 LDPE	6 PMP	7 Iodine solution (5 mg/ml)	RMSE(%)
Ground truth	6.240	4.525	3.368	3.400	3.155	2.851	3.356	
W/o noise suppression	6.158	4.127	3.882	2.984	2.729	2.274	3.370	
Average Percentage Errors E(%)	1.31%	8.80%	15.26%	12.24%	13.50%	20.24%	0.42%	12.27%
Low-pass filtration	5.999	3.318	3.025	2.716	1.809	1.232	2.190	
Average Percentage Errors E(%)	3.86%	26.67%	10.18%	20.12%	42.66%	56.79%	34.74%	32.70%
Proposed method	6.171	4.288	3.936	3.140	2.769	2.243	3.348	
Average Percentage Errors E(%)	1.11%	5.24%	16.86%	7.65%	12.23%	21.33%	0.24%	11.81%

Author Manuscript

This article is protected by copyright. All rights reserved

Table 6. The means and STDs of decomposed images within each ROI

Methods	ROI1 Bone	ROI2 Iodine	ROI3 Muscle	ROI4 Fat	ROI5 Air
W/o noise suppression	0.8652±0.1248	0.6282±0.2781	0.6623±0.2603	0.7237±0.2711	1.0000±0.0000
Low-pass filtration	0.4916±0.0159	0.6524±0.1867	0.6888±0.0272	0.7703±0.0225	1.0000±0.0000
Proposed method	0.8806±0.0056	0.7801±0.1681	0.7914±0.0194	0.8623±0.0208	1.0000±0.0000

Author Manuscript

This article is protected by copyright. All rights reserved

Table 7. The means and STDs of decomposed images within each ROI

Methods	ROI1 Bone	ROI2 Iodine	ROI3 Muscle	ROI4 Fat	ROI5 Air
W/o noise suppression	0.9719±0.0556	0.9056±0.0656	0.9382±0.0733	0.8602±0.1465	0.9735±0.0226
Low-pass filtration	0.9713±0.0554	0.8700±0.0572	0.9573±0.0210	0.8679±0.0863	0.9735±0.0226
Proposed method	0.9722±0.0524	0.9135±0.0540	0.9575±0.0161	0.8898±0.0843	0.9737±0.0222

Author Manuscript

This article is protected by copyright. All rights reserved

Table 8. The means and STDs of decomposed images within each ROI

Methods	ROI1 Bone	ROI2 Muscle	ROI3 Fat	ROI4 Air
W/o noise suppression	0.9099±0.0820	0.9451±0.1189	0.8086±0.1496	0.9801±0.0091
Low-pass filtration	0.9091±0.0379	0.9804±0.0229	0.8427±0.0400	0.9799±0.0021
Proposed method	0.9270±0.0353	0.9844±0.0199	0.8455±0.0311	0.9806±0.0020

Author Manuscript

This article is protected by copyright. All rights reserved

Table 9. The regularization coefficients and edge-preserving parameters for each study

Data	β_l	δ_l
Digital phantom (for bone, muscle, fat and air images)	0.01, 0.01, 0.1, 0.01	0.1, 0.1, 0.01, 0.1
Catphan©600 phantom (for teflon, delrin, iodine, PMP, soft-tissue and air images)	0.6, 5, 2.5, 1, 1, 7	0.005, 0.005, 0.02, 0.012, 0.012, 0.012
pelvis patient data (for bone, iodine, muscle, fat and air images)	1, 1.5, 0.9, 0.9, 0.1	0.01, 0.005, 0.01, 0.01, 0.1
head patient data (for bone, iodine, muscle, fat and air images)	0.2, 0.3, 0.09, 0.09, 0.04	0.01, 0.005, 0.01, 0.01, 0.1
thigh patient data (for bone, muscle, fat and air images)	0.03, 0.01, 0.05, 0.09	0.05, 0.08, 0.01, 0.01

Author Manuscript

This article is protected by copyright. All rights reserved

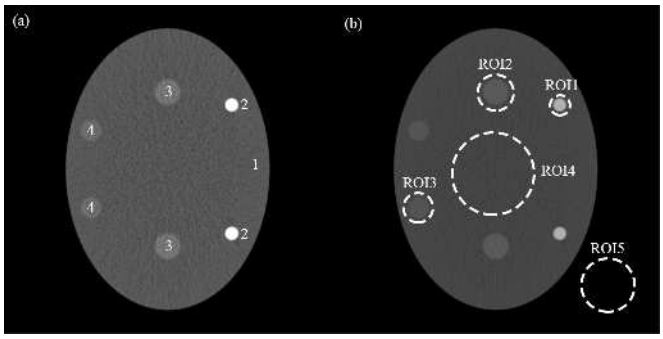

mp_12096_f7.jpg

Author Manuscript

This article is protected by copyright. All rights reserved

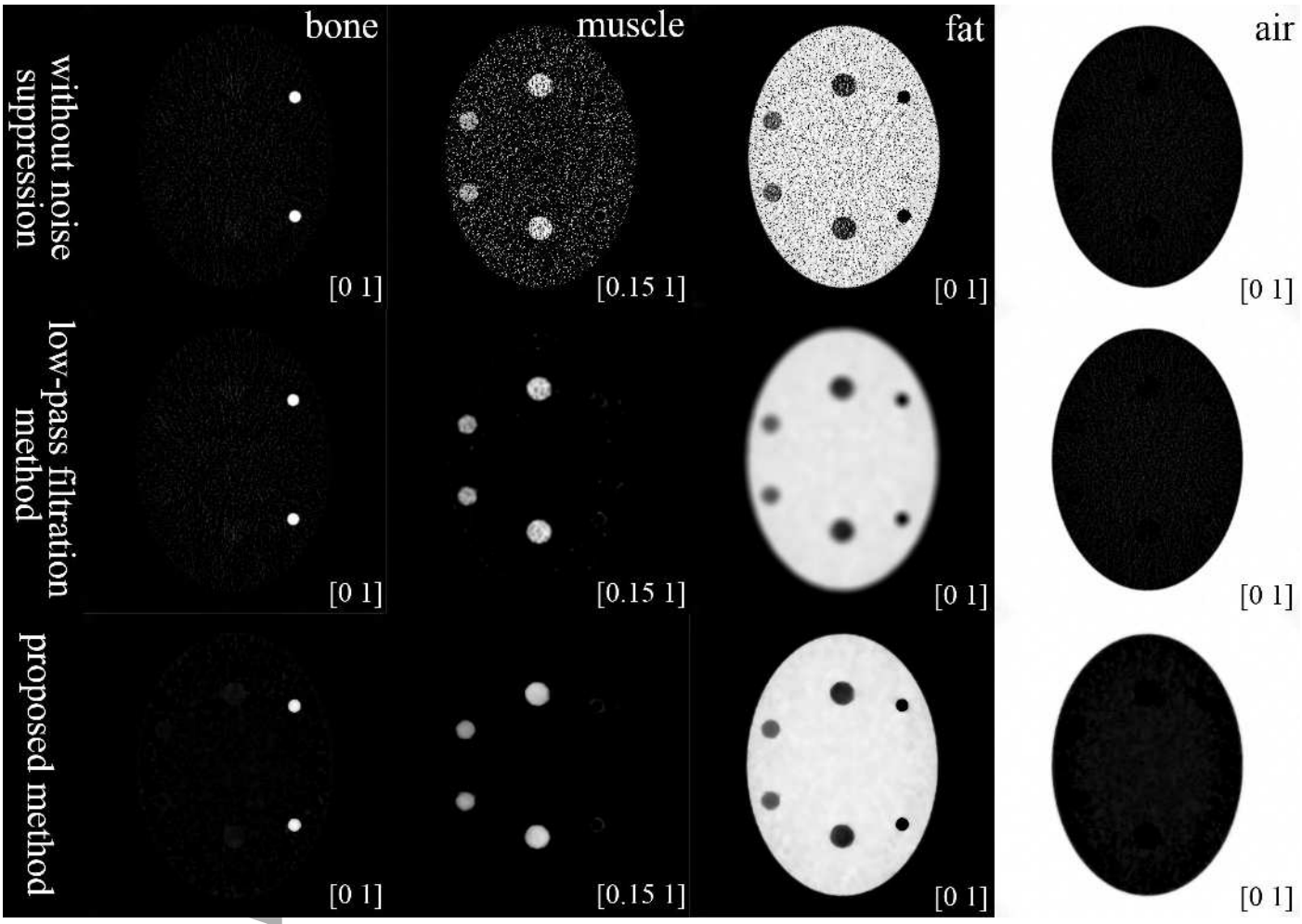

mp_12096_f8a.jpg

Author M

This article is protected by copyright. All rights reserved

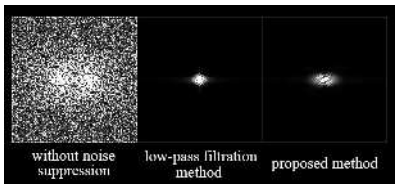

mp_12096_f8b.jpg

Author Manuscript

This article is protected by copyright. All rights reserved

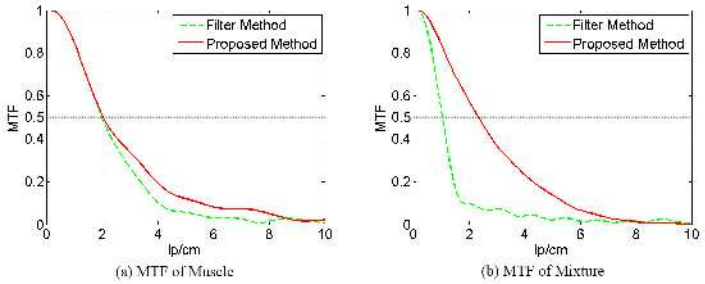

mp_12096_f9a.jpg

Author Manuscript

This article is protected by copyright. All rights reserved

Author Manuscript

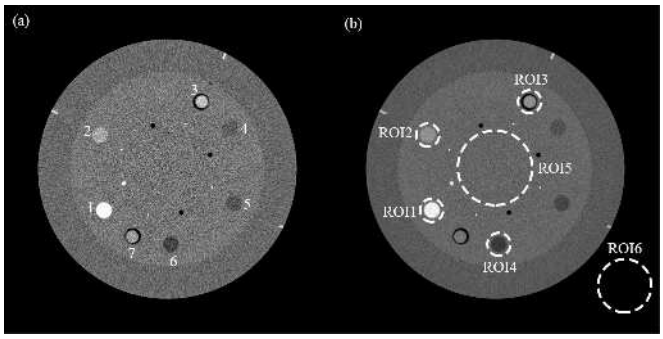

mp_12096_f9b.jpg

This article is protected by copyright. All rights reserved

Author Manuscript

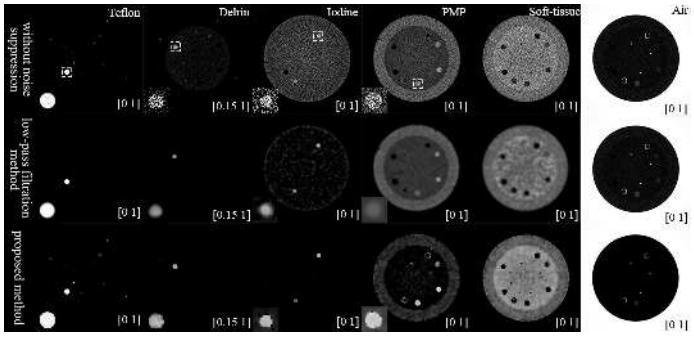

mp_12096_f10.jpg

This article is protected by copyright. All rights reserved

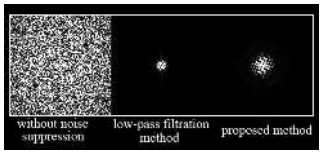

mp_12096_f11.jpg

Author Manuscript

This article is protected by copyright. All rights reserved

Author Manuscript

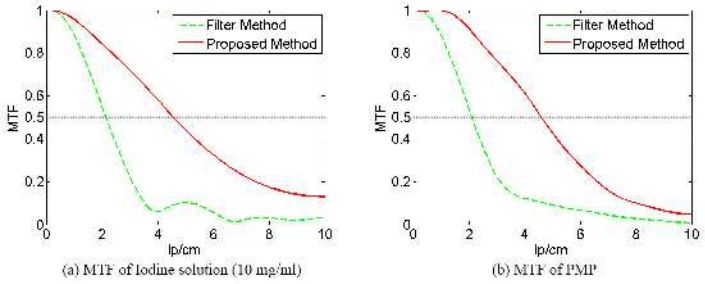

mp_12096_f12a.jpg

This article is protected by copyright. All rights reserved

Author Manuscript

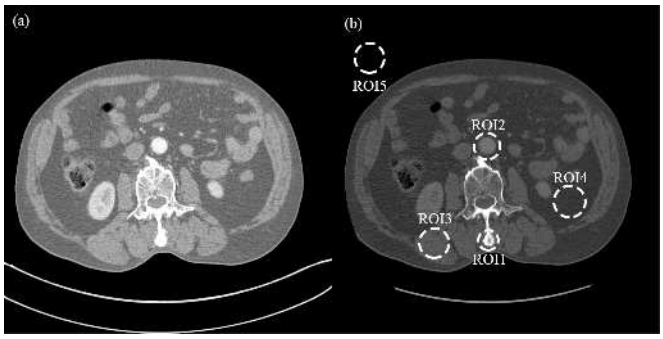

mp_12096_f12b.jpg

This article is protected by copyright. All rights reserved

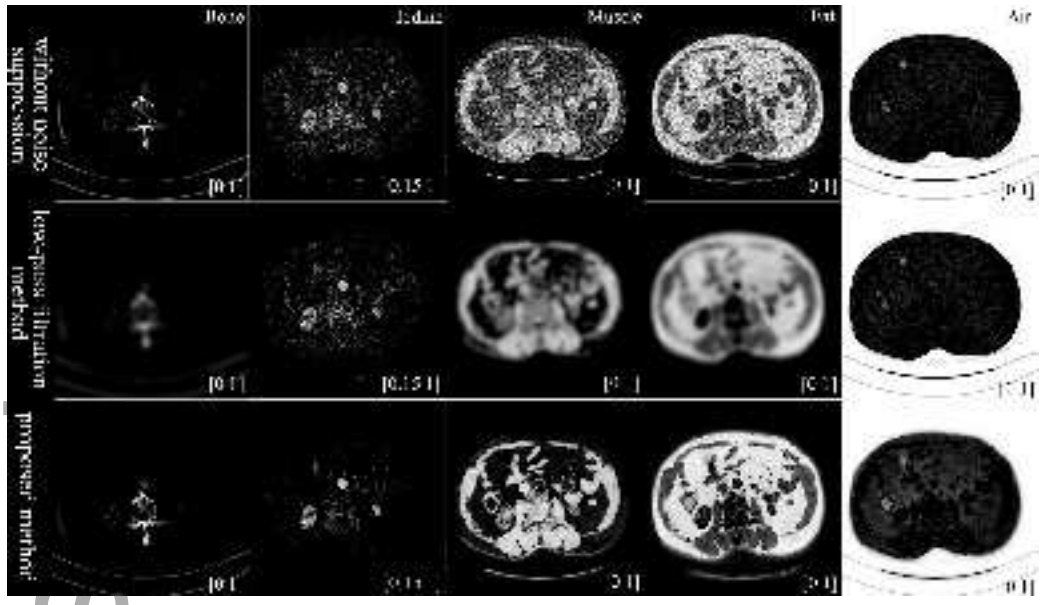

mp_12096_f13.jpg

Author Manus

This article is protected by copyright. All rights reserved

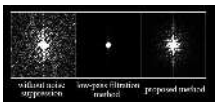

mp_12096_f14a.jpg

Author Manuscript

This article is protected by copyright. All rights reserved

Author Manuscript

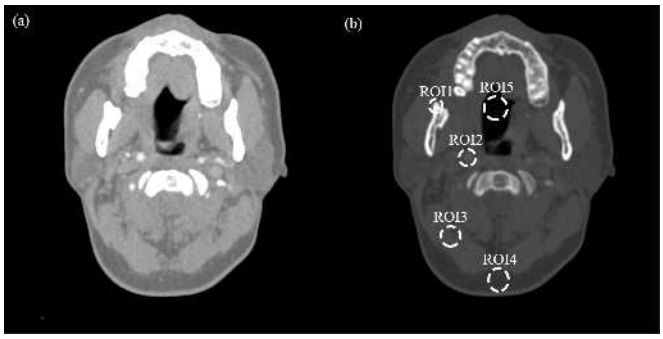

mp_12096_f14b.jpg

This article is protected by copyright. All rights reserved